A spontaneous mutation in MutL-Homolog 3 (HvMLH3) affects synapsis and crossover resolution in the barley desynaptic mutant des10

Colas, Isabelle; Macaulay, Malcolm; Higgins, James D; Phillips, Dylan; Barakate, Abdellah; Posch, Markus; Armstrong, Susan J; Franklin, F Chris H; Halpin, Claire; Waugh, Robbie; Ramsay, Luke

DOI:
10.1111/nph.14061

Title: A spontaneous mutation in MutL-Homolog 3 (HvMLH3) affects synapsis and crossover resolution in the barley desynaptic mutant *des10.*

Authors: Isabelle Colas[1], Malcolm Macaulay[1], James D. Higgins[2], Dylan Phillips[3], Abdellah Barakate[4], Markus Posch[5], Sue J. Armstrong[6], F. Chris H. Franklin[6], Claire Halpin[4], Robbie Waugh[1,4*], and Luke Ramsay[1*].

1- Cell and Molecular Sciences, The James Hutton Institute, Invergowrie, Dundee,Scotland DD2 5DA, UK.
2- University of Leicester, Adrian Building, University Road, Leicester, LE1 7R, UK.
3- Institute of Biological, Environmental and Rural Sciences (IBERS), Aberystwyth University (UK), SY23 3DA.
4- Division of Plant Sciences, University of Dundee at The James Hutton Institute, Invergowrie, Dundee, Scotland DD2 5DA, UK.
5- College of Life Sciences, Light Microscopy Facility, Dundee, Scotland DD1 5EH, UK.
6- School of Biosciences, University of Birmingham, Edgbaston, Birmingham, B15 2TT UK.

***Corresponding Authors**: Luke Ramsay and Robbie Waugh
e-mail: Luke.Ramsay@hutton.ac.uk and Robbie.Waugh@hutton.ac.uk
Tel: (44) 844 928 5428 Fax: (44) 844 928 5429

Keywords: barley, meiosis, recombination, MLH3, crossover, super resolution microscopy.

Words count

Manuscript length	6,483	Figures	8
Summary	200	Tables	1
Introduction	969	Supplementary Table	1
Materials and Methods	1,374	Supplementary Figures	10
Results	2,207	Figures in colour	All
Discussion	1,923		
Acknowledgement	110		

Summary

- Although meiosis is evolutionarily conserved, many of the underlying mechanisms show species specific differences. These are poorly understood in large genome plant species such as barley (*Hordeum vulgare* L.) where meiotic recombination is very heavily skewed to the ends of chromosomes.
- The characterisation of mutant lines can help elucidate how recombination is controlled. We used a combination of genetic segregation analysis, cytogenetics, immunocytology and 3D imaging to genetically map and characterize the barley meiotic mutant *DESYNAPTIC 10* (*des10*).
- We identified a natural exonic deletion in the ortholog of *MutL-Homolog 3* (*HvMlh3*) as the causal lesion. Compared to wild-type, *des10* mutants exhibit reduced recombination and fewer chiasmata, resulting in the loss of obligate crossovers and leading to chromosome mis-segregation. Using 3D-SIM, we observed that normal synapsis progression was also disrupted in *des10*, a phenotype that was not evident with standard confocal microscopy and that has not been reported with *Mlh3* knock-out mutants in Arabidopsis.
- Our data provide new insights on the interplay between synapsis and recombination in barley and highlight the need for detailed studies of meiosis in non-model species. This study also confirms the importance of early stages of prophase I for the control of recombination in large genome cereals.

INTRODUCTION

Meiotic recombination is one of the principal forces underlying genetic diversity and a driver for evolution as well as progress in crop breeding programmes (Riley et al, 1981). A deeper understanding of this process offers the opportunity to manipulate recombination and improve the speed and accuracy of plant breeding in order to address the needs of food security within a period of increased environmental constraints (Able et al, 2009; Martinez-Perez, 2009). This is particularly true in cereals such as wheat, barley, oats, and rye as well as in many forage grasses that show a highly skewed distribution of meiotic crossovers (CO) relative to gene content, with large portions of the chromosomes around the centromeric regions rarely recombining (Higgins et al, 2012; IBGSC et al, 2012; Kunzel et al, 2000; Kunzel and Waugh, 2002; Ramsay et al, 2014). Interestingly this CO distribution phenotype is not found in Arabidopsis nor in either rice or Brachypodium, grass species with much smaller genomes (Chen et al, 2002; Huo et al, 2011, Salomé et al, 2012). The control of recombination and the interlinked processes of early meiotic progression have been intensively studied in model eukaryotic organisms with comparative studies being undertaken in mammalian species and the standard model plants Arabidopsis and rice (Baudat et al, 2013; Gerton and Hawley, 2005; Luo et al, 2014; Mercier et al, 2014), but they have yet to be deciphered in large genome cereals.

During meiosis, homologous recombination starts with the formation of programmed DNA double-stranded breaks (DSB) by the protein SPO11 that is found in all eukaryotes (Keeney, 2008; Metzler-Guillemain and de Massy, 2000, Stacey et al, 2006). The DSB ends are resected by the MRE11 complex (MRE11-Rad50-Xrs2 in yeast, MRE11-Rad50-NSB1 in plants) to generate 3’ ssDNA tails (Daoudal-Cotterell et al, 2002; Nicolette, 2010, Raynard et al, 2008) which are then coated by the recombinases RAD51 and DMC1 to mediate strand invasion resulting in a joint molecule (D-Loop) (Shinohara et al, 1997, Da Ines et al, 2012; Kathiresan et al, 2002; Kurzbauer et al, 2012). The subsequent repair occurs either by synthesis-dependent strand annealing (SDSA) resulting in non-crossovers (NCO) or via a double Holliday junction (dHj) (Hunter, 2007; Bzymek et al, 2010, Matos and West, 2014; Bzymek et al 2010). Protein complexes (MSH4-MSH5, MER3) stabilize the dHjs (Nakagawa and Kolodner, 2002; Snowden et al, 2004;) that are mostly resolved into crossovers (CO) by the MutL homologs MLH1-MLH3 (Ranjha et al, 2014; Rogacheva et al, 2014) with a certain fraction resolved into NCO by a helicase-dependent mechanism in Arabidopsis (Knoll and

Puchta, 2011). Orthologues for many of these proteins have been identified in plants, suggesting a broadly conserved mechanism for crossover formation (Higgins et al, 2014; Luo et al, 2014; Mercier et al, 2014). It has been postulated that in Arabidopsis 85% of crossovers arise from a pathway under the control of the ZMM (ZYP, MSH, MER) group of proteins (Higgins et al, 2004; Higgins et al, 2005; Mercier et al, 2005). This pathway produces Class I COs which exhibit interference, the phenomenon where the presence of a CO reduces the probability of an additional CO in an adjacent interval with the remaining COs being Class II that do not exhibit interference (Higgins et al, 2008).

Homologous pairing, recombination and synapsis have been extensively studied, but the interdependence between these processes remains to be fully resolved and may differ between species (Santos, 1999; Zickler, 2006). In cereals, telomeres cluster during early meiosis to bring homologous chromosomes together and initiate synapsis (Colas et al, 2008; Higgins et al, 2012). During zygotene the two homologues progressively synapse along their entire length and the process is completed at pachytene (Santos, 1999; Zickler, 2006). The synaptonemal complex then disassembles but the chromosomes remain held together by chiasmata (the cytogenetic manifestation of the COs). At metaphase I the bivalents align at the equatorial plate and each of the homologous chromosomes then separates at anaphase I. A second round of cell division then follows, resulting in sister chromatid separation and the formation of haploid cells (Stack and Anderson, 2001).

While much of our current understanding has been developed in small genome models, it is now being extended to large and complex genome non-model crops such as barley, where recent cytogenetic studies have described meiotic progression and the chronology of meiotic events (Barakate et al, 2014; Higgins et al, 2012; Phillips et al, 2012). Although largely conforming to expectations, specific observations such as the clustering of the telomeres and the spatiotemporal organization of the recombination machinery differs from Arabidopsis (Armstrong et al, 2001, Barakate et al, 2014; Higgins et al, 2012; Phillips et al, 2012). Even in related grasses (e.g. barley vs. rice) there are conflicting reports of the direction of change in the number of chiasmata formed after disrupting the amount of the synaptonemal complex protein ZIPPER1 (HvZYP1/OsZEP1) (Barakate et al, 2014; Wang et al, 2010) hinting at significant functional differences between related components of the overall meiotic machinery.

To explore meiosis in a large genome crop we have been using a collection of barley *DESYNAPTIC* mutants that were determined cytologically in 1970s to have an aberrant meiotic phenotype with the presence of univalents being ascribed to premature desynapsis (Lundqvist et al, 1997). Here we have taken a classical forward genetics approach to map the spontaneous semi-sterile *DESYNAPTIC 10* (*des10*) mutant (Lundqvist et al, 1997) and identify the causal mutation as a deleted exon in the mismatch repair gene *HvMlh3.* Using a combination of genetic segregation analysis and super-resolution immuno-cytology we show that the mutation has a deleterious effect on recombination and crossing over. The unique form of the *des10* mutant allele results in the coding sequence being maintained in frame allowing immuno-fluorescent visualisation of the protein in both mutant and wild-type, providing novel insights into its importance in the very early stages of meiosis.

MATERIALS AND METHODS:

Plant material

Plants were grown under 16h of light at 18-20°C and 8h of dark at 16°C. For cytology, the cultivar (*cv.*) Bowman (wild-type) and its nearly-isogenic line BW230 (*des10*) were grown in a growth cabinet until meiosis. Anthers were checked for meiosis stage and fixed in formaldehyde. To assess the effect of *des10* on recombination, F_2 and F_3 populations derived from BW230 x *cv.* Morex were grown in a glasshouse and young leaf tissue were collected in 96 well plates for DNA extraction and genotypic analysis. Plants were grown to maturity to assess fertility.

Mapping and sequencing

Frozen plant material was disrupted in a lysis buffer using a Qiagen grinder and DNA extracted with Qiagen DNA extraction kit using an automated station QIAxtractor® (Qiagen). Initial genetic mapping utilised a custom 384 SNP genotyping array using the Illumina beadXpress platform. For mapping we used the segregation of the semi-sterile phenotype of *des10* as a Mendelian trait. Using JoinMap 4.0 (Kyazma) software, loci were assigned to linkage groups and two rounds of regression mapping used to order the loci within groups. The iterative development of custom KASPar© SNP assays (KBioscience) derived from alignments of genic sequences, known to map in this interval, were mined for polymorphism between *cvs.* Bowman and Morex, and these used to delineate the interval

containing *des10* to a single 1.02Mb BAC contig (contig_38558) containing six annotated genes (http://mips.helmholtz-muenchen.de/plant/barley/fpc/index.jsp). Primers were designed to amplify the genomic sequences of the six genes within the BAC contig and all other possible syntenic genes and the PCR products sequenced using big dye V3.1 reaction kit and analysed on an ABI Prism 3730. For cDNA sequencing mRNA from young inflorescences and anthers from BW230(*des10)* and Bowman was extracted using an RNA extraction kit (Qiagen) in presence of DNAseI. cDNA was made using the standard protocol of the Superscript III kit (Life Technologies) and sequenced using specific primers encompassing the deleted region.

Recombination frequency

F_3 individuals derived from selfed seed from F_2 individuals homozygous for *des10* or wild-type alleles at *HvMlh3* were used for the recombination assay. The genome wide genetic mapping utilised the custom 384 SNP genotyping array. Three independent ~20cM intervals on 4H (centromeric), short arm of 6H (distal) and long arm of 7H (distal) were studied in more depth using KASP© assays.

Immunocytology

Anthers were fixed in 4% formaldehyde (1X PBS/0.5% Triton™ X-100) for 20 to 30 minutes, rinsed twice in 1XPBS/0.5% Triton™ X-100 and tapped to release the meiocytes. Meiocytes suspension (30µl) were transferred onto a *Polysine® slide (Poly-L-Lysine coated slides)* and left to air dry (room temperature) and without squashing to preserve the 3D conformation. Slides were first blocked 30 minutes in 3% BSA in 1XPBS, 0.1% Triton™ X-100 and then incubated in the primary antibody solution which consisted of one or multiple antibodies (raised in rabbit or rat) diluted in blocking solution in a wet chamber for 1 hour at room temperature followed by 24-48h at 4°C. The antibodies that have been previously described were; anti-AtASY1, -AtZYP1, -HvMLH3, -AtRAD51, -AtMHS4, -AtDMC1 (Barakate et al, 2014; Higgins et al, 2012; Phillips et al, 2012; Phillips et al, 2013). We also prepared a new barley antibody, anti-HvZYP1 (Rat), from an immunization with two individual peptides (Dundee Cell Product) to confirm the ZYP1 phenotype. Slides were warmed for 30 minutes to 1 hour at room temperature before washing for 15 minutes in 1XPBS and incubating for up to 2 hours at room temperature in a secondary antibody solution consisting of a mixture of anti-rabbit Alexa Fluor® (488 or 568) and/or anti-rat Alexa Fluor® (568 or 488) (Invitrogen) diluted in 1XPBS. Slides were washed 15min in

1XPBS, counterstained with Hoechst 33342 (Life Technologies) for 15 minutes, and mounted in Vectashield® (H-1000, Vectorlabs).

DNA *in situ* hybridization

For chiasmata counts, anthers were fixed in Ethanol/Acetic acid (3:1) for 24 hours and stored in 70% Ethanol at 4°C until use. Slide preparation and DNA *in situ* hybridizations were performed as previously described (Higgins et al, 2012) using rDNA 5s-digoxigenin and rDNA 45s-biotin probes to identify the individual chromosomes.

Time course

Stems were injected with 0.5ml to 1ml of 10µM 5-ethynyl-2´-deoxyuridine (EdU) in the region of the inflorescence (under the base of the spike) and also two thirds of the way up along the length of the stem. The EdU solution was left in the stems for 2 h to allow for its incorporation into S-phase nuclei as previously described (Higgins et al, 2012). Spikes were collected and fixed in fresh 4% formaldehyde/PBS fixative for 30 minutes to 1 hour at various time-points (6, 18, 24, 48, and 68 hours after the 2 hours of EdU pulse). Fixed anthers were prepared for immuno-detection with anti-ASY1 (primary and secondary incubation) as described above, immediately followed by EdU detection as per the suppliers protocol. EdU was detected with Click-iT® EdU Alexa Fluor® 488 HCS assay kit (Life Technologies) with 45 minutes incubation instead of 30 minutes in the supplied protocol. Slides were counterstained with Hoechst 33342 (2µg/ml, Life Technologies), mounted in Vectashield® (H-1000, Vectolabs) and sealed.

Microscopy

For confocal microscopy, 3D Confocal stack images (512x512, 12bits) were acquired on a LSM-Zeiss 710 fitted C-Apochromat 63x/1.20 W Korr M27 oil objective. Laser light (405, 488, 561 and or 594nm) were used at 2-4%, sequentially with 2 (up to 4) lines averages. 3D stack slices were taken at 0.25 to 0.44 µm interval at pixel dwell 1.58 µs. For SC spreads, imaging was performed using a Nikon Eclipse 90i microscope as previously described (Higgins et al., 2012; Barakate et al, 2014). For structured illumination microscopy, 3D-SIM images were acquired on a DeltaVision OMX Blaze (GE Healthcare) fitted with an Olympus PlanApo N 60x 1.42 NA oil objective. Laser light from solid state lasers (405, 488 and 564nm), shuttered by high speed tilt mirrors and coupled into a broadband single mode optical fibre was split into three beams. 3D interference pattern in the sample plane are

generated by focusing of the beans onto the back focal plane of the objective lens. Striped illumination patters are shifted by five phase steps and rotated by 3 angles (-60˚, 0˚ and +60˚), providing a set of 15 images per unprocessed z-section. Interference patterns were phase shifted by directing the outer two beams through a separate pair of windows with individual tilt control. Phase of the interference pattern at the sample plane was shifted due to the change in the path length for the respective outer beam, while lateral refractive beam translation was canceled by tilting a given window pair in complementary directions. Angles of pattern orientation were shifted by a tilt mirror, directing the three beams pattern to one of three mirror clusters; the beam pattern from each of the three rotation paths was redirected back to a common exit path by reflecting a second time from the tilt mirror. Exposure times were typically between 100 and 200 ms, and the power of each laser was adjusted to achieve optimal intensities of between 1,000 and 3,000 counts in a raw image of 15-bit dynamic range of Edge sCMOS camera (PCO AG, Germany). The lowest possible laser power was chosen for each channel to minimize photo bleaching. Unprocessed image stacks were composed of 15 images per z-section (five phase-shifted images per each of three interference pattern angles). The microscope was routinely calibrated by measuring channel specific optical transfer functions (OTFs) to optimize lateral and axial image resolution (channel dependent and typically ~120 and ~300nm, resp.). Super-resolution three-dimensional image stacks were reconstructed with SoftWoRx 6.0 (GE) using channel specific OTFs and Wiener filter setting of 0.002 (0.005 for the DAPI channel) to generate a super-resolution three-dimensional image stack. Images from the different colour channels, recorded on separate cameras, were registered with SoftWorx 6.0 alignment tool (GE), based on alignment parameters obtained from calibration measurements with 100nm-diameter TetraSpeck beads (Life Technologies).

Imaging and modelling

Images were processed with the respective microscope software package, or with external imaging tools like Fiji (ImageJ 1.49m) for deconvolution (Schindelin et al, 2012; Vonesch and Unser, 2008) and Imaris 8.1.2 (Bitplane) for 3D projection and MLH3 counting. Barley MLH3 protein modelling was obtained by submitting the protein sequence of the intact protein and the truncated version to the SWISS-MODEL workspace (Bordoli et al, 2009).

RESULTS

des10 is the result of a mutation in the mismatch repair gene *HvMlh3*.

des10 is a spontaneous semi-sterile mutant of the barley cultivar (*cv*.) Betzes (Lundqvist et al, 1997). The original mutation was backcrossed repeatedly to *cv.* Bowman then selfed to produce the Bc_5F_3 near-isogenic line BW230 (*des10*) (Fig. 1a) (Druka et al, 2010). To identify the lesion causing the observed phenotype, we genetically mapped the *des10* mutation using an F_2 population (n=168) derived from a cross between BW230 (*des10*) and the *cv.* Morex to the long arm of chromosome 5H (Fig. 1b) using a standard SNP marker set (Close et al, 2009; Druka et al, 2011). By extending the population to 1102 F_2 plants and using additional KASP™ SNP markers developed using published genome sequence data from *cvs.* Morex and Bowman (IBGSC et al, 2012), we located *des10* to a 0.2 cM interval encompassed entirely within a 1.02 Mb BAC contig (contig_38558) containing six annotated genes (Fig. 1b). Sequencing all six genes revealed a single polymorphism between BW230 (*des10*) and Betzes in MLOC_52425 (Fig. 1b) consisting of a 159 bp deletion that removes the entire seventeenth exon of a putative gene model encoding HvMutL-homolog 3 (HvMLH3 - GenBank accession no. JQ855501, Fig. S1a), but maintaining the open reading frame of the downstream exons (Fig. S1b and Fig. 2a). The deleted exon encodes the majority of the conserved $DQHAX_2EX_4E$ metal binding motif essential for the endonuclease activity of HvMLH3 (Fig. 2b), a mismatch repair protein that has a role in the resolution of double Holliday junctions (dHj) arising from the ZMM dependent CO pathway (Jackson et al, 2006; Lipkin et al, 2000; Nishant et al, 2008; Phillips et al, 2013). Deletion of this domain is predicted to affect protein conformation (Fig. 2c-d), potentially destabilizing the MutLγ protein complex (MLH1-MLH3) required for resolution of dHjs (Guarne et al, 2004; Ranjha et al, 2014).

des10 has fewer chiasmata than observed in wild-type.

To confirm and further characterise the meiotic phenotype of *des10* mutants we used fluorescence *in situ* hybridization (FISH) with probes against 45S and 5S rDNA to determine chiasma frequencies and CO at metaphase I in wild-type and *des10*. While homologues are normally paired at pachytene in both genotypes (Fig. 3a,e), *des10* exhibits fewer chiasmata. In the wild-type metaphase I, the number of chiasmata ranged from 16 to 20 per nucleus with the mean frequency of 18.4±1.3 (n=21) (Fig. 3b,i,j) slightly lower than CO numbers

(mean=21.8) estimated from genetic maps (Close et al, 2009; IBGSC et al, 2012) but closer than previous estimates (Nilsson et al, 1993). In *des10* we observed significantly fewer chiasmata ranging from 5 to 13 per nucleus with a mean of 9.2±2.1 (n=57) (Fig. 3f,i,j) and we also observed the presence of univalents (1.7 ± 2.0, n = 57) (Fig. 3f,i) leading to occasional aberrant chromosome segregation at anaphase I (Fig. 3c,g), genetically unbalanced tetrads (Fig. 3d,h) and a subsequent semi-fertile phenotype. Given the similar size of the seven chromosome pairs, the distribution of chiasmata per nucleus in *des10* can be compared to that expected assuming a Poisson distribution of the number of chiasmata observed (Jones, 1967). The observed distribution was significantly different from that expected from a random distribution (p=0.034), which indicated that although the presence of univalents is indicative of a substantial disruption, some control of CO distribution remained (Jones, 1967, Jackson et al, 2006).

***des10* shows reduced genetic recombination frequency**.

Given the recessive nature of the mutation we investigated the effect of *des10* on genetic recombination using segregating F_3 families derived from specific F_2 individuals from the BW230 (*des10*) x Morex cross that were homozygous for either the wild-type (n=188 across 15 F_2 familes) or *des10* mutant (n=183 across 16 F_2 familes) allele at *HvMlh3*. The reconstituted chromosome linkage maps generated from the segregation data within the F_3 families derived from wild-type F_2 individuals were comparable to the barley consensus map (Close et al, 2009; IBGSC et al, 2012). However the maps derived from the segregation data within the F_3 families derived from *des10* F_2 individuals showed considerably less recombination, being only 45.9% of the length of the maps derived from wild-type families (excluding chromosome 5H due to the selection at the *HvMlh3* locus) (Fig. 4, Fig. S2). There was little evidence to suggest that the reduction in recombination varied across the genome with similar reductions observed in subtelomeric (44.2%) or centromere-proximal regions (51.4%) (Fig. S2) with the estimates of genetic to physical distance ratios in wild-type and *des10* changing from 1.16 to 0.46 cM/Mb in distal subtelomeric regions and from 0.06 to 0.03 cM/Mb in proximal regions . The reduction in recombination frequency was confirmed by comparisons at three specific intervals delineated by KASP SNP markers on a larger number of individuals from F_3 families (wild-type, n=695 across 22 F_2 familes; *des10*, n=556 across 24 F_2 familes) that all showed a significant differences in recombination with *des10* lines showing an mean reduction to 39% wild-type recombination frequency (26.0-54.6%

($p=8.4^{e-8}$-0.01) (Fig. S3). The reduction in recombination in these F_3 families paralleled the reduction of chiasmata observed cytogenetically in the mutant *des10* compared to wild-type.

Chromosome pairing is normal but the normal progression of synapsis appears compromised in *des10.*

Given the importance of the interplay between synapsis and recombination in CO formation (Santos, 1999, Zickler, 2006), we compared synapsis in *des10* and wild-type using antibodies raised against AtZYP1 and the axial element associated protein AtASY1 (Barakate et al, 2014; Higgins et al, 2012; Phillips et al, 2012) using Structured Illumination Microscopy (SIM). Axis formation and the initiation of synapsis during leptotene were comparable in wild-type (Fig. 5a-b and Fig. S4) and *des10* (Fig. 5g-h and Fig. S4). By mid-zygotene in wild-type most of the chromosomes were paired (Fig. 5c,d) and the typical tri-partite structure of the SC was visible (Fig. 5d, white arrow) with the ZYP1 signal suggesting new synapsis initiation sites as shown previously (Phillips et al, 2012). The tri-partite structure is also clearly visible at pachytene in wild-type with complete synapsis evident (Fig. 5e,f). Using confocal-microscopy, synapsis appeared to progress normally with the linearization of the ZYP1 signal during zygotene-pachytene (Fig. S5). However with SIM there appeared to be a difference in the relative positioning of ZYP1 compared to wild-type with a highly punctate ZYP1 signal observed in *des10* at mid zygotene (Fig. 5i,j) or later (Fig. 5k,l) that precluded the discernment of the SC tri-partite structure at mid-zygotene (Fig. 5j) or late zygotene/pachytene (Fig. 5l). The problems of homologue pairing were also indicated by unsynapsed ASY1 regions resembling the previously described “peg and coalescent” process (Colas et al, 2008) at early zygotene in *des10* (Fig. 5j, arrows). However the punctuated appearance of ZYP1 seen with SIM was not obvious when using confocal images, where the ZYP1 signal appeared linear in *des10* (Fig. S5). This suggests that the homologous chromosomes are aligned but that either the SC is not fully mature in the mutant or that in *des10* the chromatin structure is altered precluding binding of the ZYP1 antibody. Using Imaris we were able to track the individual bivalents of the later zygotene/pachytene cells in *des10* (Figure 5k) and show that the distance between the ASY1 labelled homologues were maintained at 0.1µm (Figure 6) as previously reported at pachytene (Phillips et al, 2012) suggesting that despite the non-linear ZYP1 these cells are fully synapsed.

des10 displays delayed synapsis.

The observations of a perturbed synaptic progression were unexpected given that synapsis has been reported as normal in both Arabidopsis and mouse knock-out *mlh3* mutants (Jackson et al, 2006; Lipkin et al, 2002) albeit that these have not been analysed using 3D-SIM. In order to better understand how and when the mutation in *des10* was having this effect, we conducted a time course analysis using 5-ethynyl-2´-deoxyuridine (EdU) labelling. After collecting spikes of the same size in both wild-type and *des10* for each time point, meiocytes were spread from the central spikelets (numbers 3 to 10). This enabled several stages of meiosis to be studied for each spike with the EdU intensity/distribution and ASY1 linearity/intensity under confocal microscopy being used to classify the cells. A total of 27, 163, 98 and 141 cells were counted at 18h, 24h, 48h and 68h respectively in the wild type and 26, 172, 167 and 46 cells were counted at 18h, 24h, 48h and 68h respectively in *des10*. We observed that early meiotic events in *des10* were comparable to wild-type with the presence of the telomere bouquet, which produces a concentrated ASY1 signal at one side of the nucleus (Higgins et al, 2012), at 6h (Fig. 7a-c) and 18h (Fig. 7d-f). However by 48 hours (Fig. 7j-l) while in wild-type there were roughly equal numbers of cells in zygotene and pachytene with 8% in later stages, in *des10*, 87% of the total cells were in zygotene with no cells found at pachytene, although 5% were at later stages. This result corresponds to the apparent defect in synapsis described above suggesting that in *des10*, cells appear suspended at zygotene with very few exhibiting a mature pachytene (with a strong linear ZYP1 signal relating to chromosome condensation). At 68h (Fig. 7m-o), similar levels of metaphase I were found in wild-type and *des10*, but while 100% of them are labelled in wild-type, 29% of the total metaphase I cells were not labelled in *des10*, indicating that in *des10* they have lost synchronicity, potentially due to the delay in synapsis. Although this lack of synchronicity made estimates difficult for the majority of the cells, the total length of prophase does not appear generally different between wild-type and *des10*. Thus, unlike the 25 hours delay in reaching metaphase I in knock-out *AtMlh3* mutants (Jackson et al, 2006), *des10* cells exhibit no overall (or little) time delay compared to wild-type. Moreover, a comparison of the stages of meiotic progression relative to changes in meiocyte size based on DNA staining (Fig. S6) revealed that the expected chromosomal changes were delayed in *des10* relative to wild-type (Higgins et al, 2012; Jackson et al, 2006; Kleckner et al, 2004).

HvMLH3 foci detectable in wild-type and *des10*

Using high resolution immuno-cytology, we observed that the HvMLH3 antibody (Phillips et al, 2013) produced a punctate signal associated with the nucleus at zygotene in wild-type barley with some MLH3 signal associated with chromatin and the forming SC (Fig. 8a-d). At late zygotene/early pachytene, synapsis of the chromosomes in wild-type progressed via ZYP1 polymerization and although the MLH3 signals are detectable in the nucleus, a subset of more distinct MLH3 foci become evident on the SC (Fig. 8e-h, triangles). At late pachytene, (Fig. 8i-l), polymerization of ZYP1 is complete and distinct MLH3 foci are evident as previously described (Phillips et al, 2013). Using 3D stacks, the final MLH3 foci count (Fig. 8j, triangles and Fig. S7) averaged 20.8 (± 3.4, n=19) per cell (Table S1) for the wild-type, which closely corresponds to the average chiasma count of 18.4 at metaphase I.

The exonic deletion in *des10* almost entirely removes the functional HvMLH3 metal binding motif but as the mutation left *HvMlh3* in frame, it potentially produces detectable protein that is endonuclease deficient and under the control of its native promoter. This was confirmed with immuno-cytology with the HvMLH3 antibody in conjunction with HvZYP1 allowing the observation of the mutant protein in relation to the synaptonemal complex formation. As the problems of synapsis in *des10* that are evident when using 3D-SIM could complicate accurate staging when using the ZYP1 antibody without ASY1, the staging was also carried out using confocal images where the ZYP1 signal appears linear in *des10* (Fig. S5).

At zygotene, we observed a similar MLH3 signal in the nucleus in *des10* (Fig. 8m-p) as in the wild-type (Fig. 8a-d). However at late zygotene/pachytene, judged by the stage of ZYP1 polymerization, distinct foci are much less apparent in *des10* (Fig. 8q-t) with a higher background MLH3 signal present in the nucleus (Fig. 8t). At the pachytene-like stage in *des10*, distinct foci do form and the final number could be estimated using 3D image stacks (Fig. 8v, triangles and Fig. S8) with the mean being 7.7 foci/cell (± 1.6, n=30) (Table S1) which is close to the observed average of 9.2 chiasmata per nucleus. The distribution of the number of MLH3 foci per nucleus in *des10* was significantly different from a Poisson distribution (p=0.011), confirming our earlier conclusion from chiasmata counts that the COs are not random (Jackson et al, 2006). Interestingly although the number of cells was limited and the count subject to experimental error, the MLH3 foci distribution in *des10* did however just fit a binomial distribution expected given the number of foci found in the mutant and wild-type.

In addition, we found that DSB formation was not disturbed in *des10* and progressively formed in both wild-type and *des10* from the distal regions and localized to the axial elements as previously described in barley (Fig. S9 and S10) (Barakate et al, 2014; Higgins et al, 2012; Phillips et al, 2012). However, higher numbers of RAD51, DMC1 and MSH4 foci were found in *des10*, compared to the wild-type, (Table 1, Fig. S9 and S10) suggesting that the mutation is either affecting DSB numbers as previously reported in ZMM mutants (Thacker et al, 2014), or the dynamics of DSB repair.

DISCUSSION

des10 is a spontaneous mutation in *HvMlh3*

Using classical forward genetics we show that the spontaneous semi-sterile barley *des10* mutant is the consequence of a deletion of exon 17 of *MutL-homolog 3* (Hv*Mlh3*) that contains most of the conserved C-terminal metal binding endonuclease domain. The *des10* mutant showed a clear meiotic phenotype with a reduction in chiasmata number relative to wild-type that mirrors the reduction seen in the knock-out mutants in Arabidopsis, the only other plant for which *mlh3* mutants have been characterised (Jackson et al, 2006). As in Arabidopsis, the presence of some univalents indicates that the remaining COs are insufficient in number in some cells to ensure accurate chromosome segregation.

This similar level of reduction in chiasmata in the MLH3 mutants indicates that, as expected, the deletion of the majority of the conserved metal binding motif essential for the endonuclease activity (Nishant et al, 2008) in *des10* mimics the complete knock-out of the gene. The effects observed were however less severe than those found in classical ZMM mutants in Arabidopsis and *Zyp1* knockdowns in barley (Higgins et al, 2004; Barakate et al 2014) which also corresponds with the phenotypes observed in Arabidopsis MLH1 and MLH3 mutants (Dion et al, 2007; Jackson et al, 2006). Importantly given the nature of the mutation we were able to count the MLH3 foci directly in both wild-type and in *des10* unlike in the Arabidopsis and mouse knockout studies. These MLH3 foci counts confirmed the reduction observed with chiasmata counts, showing a reduction to 37% (7.7/20.8) compared to wild-type that mirrored the estimates of chiasmata counts (50%: 9.2/18.4) and interestingly close to the ratio found with chiasmata counts in Arabidopsis (39%) (Jackson et al, 2006).

This mutant phenotype in both species is consistent with a post-ZMM role for MLH3 in the resolution of predetermined CO sites (Jackson et al, 2006, Zakharyevich et al, 2010). This interpretation was supported in Arabidopsis by the fit of the mutant cell chiasmata frequencies to a binomial distribution that modelled the probability (p) of the independent resolution of dHjs as COs at each of a preselected set of (k) recombination intermediates. However in Arabidopsis, the chiasmata frequencies also fitted a simpler discrete Poisson distribution about the mean, potentially indicative of the random nature of the remaining COs. Importantly this simpler random distribution was not supported in this study with both the counts of chiasmata and MLH3 foci in *des10* being significantly different from the expected Poisson distributions while the MLH3 foci distribution in *des10* did only just fit a binomial distribution expected given the number of foci found in the mutant and wild-type.

The effect of *des10* was observed genetically on recombination frequency with the F_3 map length of families derived from F_2 individuals homozygous for the *des10* allele at *HvMlh3* being 45.9% the map length of wild-type. Interestingly there was little evidence to suggest that the reduction in recombination varied across the genome despite the known temporal-spatial control of recombination in barley (Higgins et al 2012). This observation corresponds well with the assumption that MLH3 is involved in the resolution of predefined CO intermediates derived from ZMM pathway and thus *des10* should not affect the distribution of designated CO events but will affect the proportion of these that are resolved as CO, i.e. will affect recombination frequency but not recombination distribution.

Intriguingly a similar proportion of wild-type CO was observed in *des10* (37%) as in AtMLH3 knockouts (39%). While the mechanism by which the dHJs are resolved in the absence of a functional MLH3 is unclear (Jackson et al 2003), the involvement of other complexes such as MLH1-PMS2 have been suggested (Lipkin et al, 2002). Considering the interaction between the MLH1-MLH3 complex and MMS4-MUS81 in yeast (de los Santos et al, 2003; Fabre et al, 2003; Wang and Kung, 2002), and the known involvement of MUS81 in mammalian (Holloway et al, 2008) and plant CO resolution (Higgins et al, 2008a), it is possible that the resolution of the Class I COs in MLH3 mutants is mediated via the Class II machinery while maintaining the ZMM CO designations and interference (Zakharyevich et al, 2010).

HvMLH3 foci evident at zygotene

The development of MLH3 foci with the developing SC at zygotene is earlier than the classical expectation, where SC associated foci are generally observed at pachytene on completion of synapsis (Lipkin et al, 2002). However this early development of MLH3 foci during zygotene is supported by observations in mouse and Arabidopsis (Kolas et al, 2005; Jackson et al 2006) and of other MutL homologs in other species (Baker et al, 1995;; Storlazzi et al, 2010). The earlier association of MLH3 signal with the nucleus at zygotene before the appearance of clear foci was surprising but showed a punctate but regular organisation of stretches of ZYP1 signal separated by MLH3 foci (Fig. 7d). This would suggest that our observations are unlike the association with heterochromatic repeats found in mouse (Baker et al, 1995) or with chromatin organization suggested during chromosome segregation in humans (Roesner et al, 2014). This would therefore indicate that MLH3 is recruited earlier to the newly formed axes potentially during synapsis, rather than on mature chromosomes axes, as suggested by animal studies reporting the presence of MLH3 at pachynema.

In *des10*, the mutation affects the dimerization domain of HvMLH3 that would potentially cause a change in the conformation of the C-terminal domain and thus possible difficulties in forming the heterodimer with MLH1 that is required for the resolution of dHJs (Guarne et al, 2004; Ranjha et al, 2014; Rogacheva et al, 2014). However the capacity of the complex to bind to chromatin would likely to be unaffected given the intact DNA binding domain, and as HvMLH3 is still recruited to the axis, its DNA binding activity appears to remain effective. This would parallel the behaviour of the yeast mutant MLH3Δ7 that also lacks the endonuclease motif, but is normally recruited to the DNA (Roesner et al, 2013). Interestingly the MLH3Δ7 studies also showed a higher turnover of the protein in the mutant that could tally with the higher background and staining of the nucleolus in this study. The early meiotic effects seen in *des10* may therefore be a manifestation of the timing of the binding of MLH3 with the continued presence of the defective protein on the axis generating a phenotype not detected in a knockout (Jackson et al, 2006; Lipkin et al, 2002)

des10 displays altered synapsis progression

The barley *des10* phenotype revealed a perturbation in the progression of synapsis compared to the wild-type that became evident at zygotene. This unexpected effect on synapsis and the associated delay in meiotic progression is broadly similar to phenotypes observed for ZMM mutants (Barakate et al, 2014; Higgins et al, 2004; Novak et al, 2001) although not as severe.

Assembled ZYP1 appears to be fairly linear under confocal microscopy and subsequent meiotic progression indicates that the chromosome are sufficiently aligned to allow some crossover resolution. However with structured illumination microscopy ZYP1 did show a less continous signal than wild-type and was associated with a longer zygotene/pachytene transition in *des10*. While the observed differences in synapsis could have been exacerbated by an increased sensitivity of the mutant protein containing complexes to the cytological procedures, such effects would *de facto* imply a change in structure. The observed perturbation of synapsis was consistent with the timing of the appearance of MLH3 signal and potentially relates to the changed binding dynamics of the mutant protein. Similarly the delay at zygotene observed in *des10* cells would be concomitent with the observed changes in structure associated with ZYP1 signal and the difficulty in observing cells with a classic pachytene appearance given the apparent problems of synapsis. It is thus unclear whether full synapsis is achieved in this desynaptic mutant or how many cells achieve full synapsis although cells clearly do progress through to diplotene.

The interplay between recombination and synapsis is a standard feature of meiotic mutant studies and is inherent in the grouping of ZIP1 (ZYP1) and mismatch repair genes in the ZMM pathway (Mercier et al, 2014; Osman et al, 2011). However the processes of recombination and synapsis are not inseparable, with DSB formation and CO imposition known to occur prior to synapsis in some species (Fung et al, 2004; Santos, 1999; Thacker et al, 2014). While our data show that CO imposition is retained in *des10*, it also suggests that SC progression is dependent on accurate CO resolution. Synapsis would therefore appear to involve different stages; with chromosome engagement, alignment and initiation being ZMM dependent (Thacker et al, 2014) but progression and maturation also being dependent on subsequent CO resolution by MLH3. We noted that RAD51/DMC1 counts were higher in *des10* and attribute this to the concomitant change in the observed timing of meiotic progression rather than a direct effect on DSB formation, as seen in ZMM mutants (Thacker et al, 2014). The observed difference in timing of MLH3 action compared to Arabidopsis could reflect the specific nature of the *des10* mutation combined with the advantages of visualising in a large genome with high resolution microscopy. Whether our observations reflect an earlier role for MLH3 in plants in general or specifically in barley, they are consistent with the known spatio-temporal difference between barley and Arabidopsis in early meiosis and the considerable variation in genome size and organisation of heterochromatin between these species (Higgins et al, 2012). There are differences in

chromosome dynamics of the two species in early prophase (Armstrong et al, 2001) with barley exhibiting a temporal differentiation in recombination initiation between distal and interstitial chromosomal regions that correspond to the relative timing of replication and the differentiation of the genome by chromatin modifications (Higgins et al, 2012; Baker et al, 2015).

In summary we have taken advantage of genetic and genomic resources in barley to identify an exonic deletion in the orthologue of *MutL-Homolog 3* (*Mlh3*) as the causal lesion in a natural semi-sterile *DESYNAPTIC 10* (*des10*) mutant. *des10* exhibits reduced recombination and fewer chiasmata than the wild-type, congruent with our expectations for the post-ZMM role of HvMLH3 in the resolution of predetermined CO sites. The reduction in chiasmata resulted in the loss of obligate crossing-over leading to chromosome mis-segregation and the semi-sterile phenotype. This study thus confirms the conserved role of MLH3 in barley previously assumed in earlier studies (Phillips et al, 2013) and the non-random nature of the CO distribution in the mutant as postulated but not demonstrated in Arabidopsis (Jackson et al, 2003). Importantly, in barley MLH3 foci are evident at zygotene, earlier than expected, although this has been observed in other systems (Kolas et al, 2005) and that using 3D-SIM super-resolution microscopy we were able to observe that *des10* also exhibited aberrant synaptonemal complex progression at this stage, associated with a meiotic delay. We interpret this as meaning that the resolution of CO is initiated early in barley and that its disruption in *des10* compromises synapsis progression with the associated change in the dynamics of the mutant MLH3 protein. Thus, in barley both crossover imposition and crossover resolution occur prior to full synapsis, affirming the importance of the early stages of prophase I for the control of recombination. The integration of genetic and cytological approaches to dissect the mutant phenotype of *Hvmlh3* establishes the tractability of studying meiosis in large genome cereals. The size of the genome facilitates cytological discrimination of the profound changes in chromosome structure during prophase I and is potentially associated with specific changes in timing of meiotic processes when compared to physically smaller model systems.

ACKNOWLEDGEMENTS

We would like to thank Sybille Mittmann, Amritpal Sandhu and Ruth Perry for technical help. The research leading to these results has received funding from the European Community's Seventh Framework Programme *FP7/2007-2013* under grant agreement n°

222883 to R.W, S.J.A and F.C.H.F. Use of the OMX microscope was supported by the Euro-BioImaging PCS and through the MRC Next Generation Optical Microscopy Award (Ref: MR/K015869/1) to I.C. L.R., M.M. and R.W. were funded from the Scottish Government's Rural and Environment Science and Analytical Services Division Work Program 5.2. A.B. and C.H were funded by the Biotechnology and Biological Science Research Council Grant BB/F020872/1. The authors declare no conflict of interest.

AUTHORS CONTRIBUTIONS:

I.C., L.R., and R.W designed the study. I.C., M.M., J.D.H, D.P., and L.R. and carried out experiments and analysis. A.B. cloned and sequenced the full-length HvMLH3 cDNA and provided resources and supervision for cDNA sequencing. M.P. carried out 3D-SIM imaging and reconstruction. M.P., A.B., C.H., S.J.A. and F.C.H.F. advised on experiment and/or manuscript revisions. I.C., R.W., A.B., F.C.H.F, S.J.A, C.H. and L.R. wrote the paper.

REFERENCES

Able, J.A., Crismani, W., and Boden, S.A. (2009). Understanding meiosis and the implications for crop improvement. Funct. Plant Biol. **36:**575-588.

Armstrong SJ, Franklin FC, and Jones GH. (2001) Nucleolus-associated telomere clustering and pairing precede meiotic chromosome synapsis in Arabidopsis thaliana. J Cell Sci. 114(Pt 23):4207-17.

Baker, K., Dhillon, T., Colas, I., Milne, I., Milne, L., Bayer M. and Flavell A.J. (2015) Chromatin state analysis of the barley epigenome reveals a higher-order structure defined by H3K27me1 and H3K27me3 abundance. Plant J. **84**: 111-124.

Baker, S.M., Bronner, C.E., Zhang, L., Plug, A.W., Robatzek, M., Warren, G., Elliott, E.A., Yu, J., Ashley, T., Arnheim, N., et al, (1995). Male mice defective in the DNA mismatch repair gene PMS2 exhibit abnormal chromosome synapsis in meiosis. Cell **82**:309-319.

Barakate, A., Higgins, J.D., Vivera, S., Stephens, J., Perry, R.M., Ramsay, L., Colas, I.,Oakey, H., Waugh, R., Franklin, F.C., et al, (2014). The synaptonemal complex protein ZYP1 is required for imposition of meiotic crossovers in barley. Plant Cell **26**:729-740.

588 **Baudat, F., Imai, Y., and de Massy, B.** (2013). Meiotic recombination in mammals:
589 localization and regulation. Nat. Rev. Gen**. 14**:794-806.
590 **Bordoli, L., Kiefer, F., Arnold, K., Benkert, P., Battey, J., and Schwede, T.** (2009).
591 Protein structure homology modeling using SWISS-MODEL workspace. Nat. Protoc.
592 **4**:1-13.
593 **Bzymek, M., Thayer, NH., Oh, SD., Kleckner, N., Hunter, N.** (2010) Double Holliday
594 junctions are intermediates of DNA break repair. Nature **8**;464(7290):937-41
595 **Chen, M.S., Presting, G., Barbazuk, W.B., Goicoechea, J.L., Blackmon, B., Fang, F.C.,**
596 **Kim, H., Frisch, D., Yu, Y.S., Sun, S.H., et al,** (2002). An integrated physical and
597 genetic map of the rice genome. Plant Cell **14**:537-545.
598 **Close, T.J., Bhat, P.R., Lonardi, S., Wu, Y.H., Rostoks, N., Ramsay, L., Druka, A.,**
599 **Stein, N., Svensson, J.T., Wanamaker, S., et al,** (2009). Development and
600 implementation of high-throughput SNP genotyping in barley. Bmc Genomics **10**:582
601 **Colas, I., Shaw, P., Prieto, P., Wanous, M., Spielmeyer, W., Mago, R., and Moore, G.**
602 (2008). Effective chromosome pairing requires chromatin remodeling at the onset of
603 meiosis. Proc Natl Acad Sci *U S A* **105**:6075-6080.
604 **Da Ines, O., Abe, K., Goubely, C., Gallego, M.E., and White, C.I.** (2012). Differing
605 Requirements for RAD51 and DMC1 in Meiotic Pairing of Centromeres and
606 Chromosome Arms in Arabidopsis thaliana. Plos Gen. **8**:245-256.
607 **Daoudal-Cotterell, S., Gallego, M.E., and White, C.I.** (2002). The plant Rad50-Mre11
608 protein complex. Febs Lett **516**:164-166.
609 **de los Santos, T., Hunter, N., Lee, C., Larkin, B., Loidl, J., and Hollingsworth, N.M.**
610 (2003). The Mus81/Mms4 endonuclease acts independently of double-holliday
611 junction resolution to promote a distinct subset of crossovers during meiosis in
612 budding yeast. Genetics **164**:81-94.
613 **Dion, E., Li, L., Jean, M., and Belzile, F.** (2007). An Arabidopsis MLH1 mutant exhibits
614 reproductive defects and reveals a dual role for this gene in mitotic recombination.
615 Plant J. **51**: 431-40.**Druka, A., Franckowiak, J., Lundqvist, U., Bonar, N.,**
616 **Alexander, J., Houston, K., Radovic, S., Shahinnia, F., Vendramin, V.,**
617 **Morgante, M., Stein, N., and Waugh R.** (2011). Genetic dissection of barley
618 morphology and development. Plant Physiology **155**:617-627.
619 **Fabre, F., Chan, A., Heyer, W.D., and Gangloff, S.** (2003). Alternate pathways involving
620 Sgs1/Top3, Mus81/Mms4, and Srs2 prevent formation of toxic recombination

intermediates from single-stranded gaps created by DNA replication. Proc Natl Acad Sci *U S A* **100**:1462-1462.

Fung, J.C., Rockmill, B., Odell, M., and Roeder, G.S. (2004). Imposition of crossover interference through the nonrandom distribution of synapsis initiation complexes. Cell **116**:795-802.

Gerton, J.L., and Hawley, R.S. (2005). Homologous chromosome interactions in meiosis: Diversity amidst conservation. Nat. Rev. Gen. **6**:477-487.

Guarne, A., Ramon-Maiques, S., Wolff, E.M., Ghirlando, R., Hu, X.J., Miller, J.H., and Yang, W. (2004). Structure of the MutL C-terminal domain: a model of intact MutL and its roles in mismatch repair. Embo J **23**:4134-4145.

Higgins, J.D., Armstrong, S.J., Franklin, F.C., and Jones, G.H. (2004). The Arabidopsis MutS homolog AtMSH4 functions at an early step in recombination: evidence for two classes of recombination in Arabidopsis. Genes Dev **18**:2557-2570.

Higgins, J.D., Buckling, E.F., Franklin, F.C., and Jones, G.H. (2008). Expression and functional analysis of AtMUS81 in Arabidopsis meiosis reveals a role in the second pathway of crossing-over. Plant J **54**:152-162.

Higgins, J.D., Osman, K., Jones, G.H., and Franklin, F.C. (2014). Factors Underlying Restricted Crossover Localization in Barley Meiosis. Annu Rev Genet **48**:29-47.

Higgins, J.D., Perry, R.M., Barakate, A., Ramsay, L., Waugh, R., Halpin, C., Armstrong, S.J., and Franklin, F.C. (2012). Spatiotemporal asymmetry of the meiotic program underlies the predominantly distal distribution of meiotic crossovers in barley. Plant Cell **24**:4096-4109.

Higgins, J.D., Sanchez-Moran, E., Armstrong, S.J., Jones, G.H., and Franklin, F.C. (2005). The Arabidopsis synaptonemal complex protein ZYP1 is required for chromosome synapsis and normal fidelity of crossing over. Genes Dev **19**:2488-2500.

Holloway, J.K., Booth, J., Edelmann, W., McGowan, C.H., and Cohen, P.E. (2008). MUS81 Generates a Subset of MLH1-MLH3-Independent Crossovers in Mammalian Meiosis. PloS Genet. **4**(9):e1000186. doi: 10.1371/journal.pgen.1000186

Hunter, N. (2007) Meiotic Recombination. Aguilera A., and Rothstein R. (eds), Springer Berlin Heidelberg, starts p381.

Huo, N.X., Garvin, D.F., You, F.M., McMahon, S., Luo, M.C., Gu, Y.Q., Lazo, G.R., and Vogel, J.P. (2011). Comparison of a high-density genetic linkage map to genome features in the model grass Brachypodium distachyon. Theor. Appl. Gen. **123**:455-464.

655 **IBGSC, Mayer, K.F.X., Waugh, R., Langridge, P., Close, T.J., Wise, R.P., Graner, A., Matsumoto, T., Sato, K., Schulman, A., et al,** (2012). A physical, genetic and functional sequence assembly of the barley genome. Nature **491**:711-716.

658 **Jackson, N., Sanchez-Moran, E., Buckling, E., Armstrong, S.J., Jones, G.H., and Franklin, F.C.H.** (2006). Reduced meiotic crossovers and delayed prophase I progression in AtMLH3-deficient Arabidopsis. Embo J **25**:1315-1323.

661 **Jones, G.H.** (1967) The control of chiasmata distribution in rye . Chromosoma 22:69-90

662 **Kathiresan, A., Khush, G.S., and Bennett, J.** (2002). Two rice DMC1 genes are differentially expressed during meiosis and during haploid and diploid mitosis. Sex. Plant Reprod. **14**:257-267.

665 **Keeney, S. (**2008). Spo11 and the Formation of DNA Double-Strand Breaks in Meiosis. Genome Dyn. Stab **2**:81-123.

667 **Kleckner, N., Zickler, D., Jones, G.H., Dekker, J., Padmore, R., Henle, J., and Hutchinson, J.** (2004). A mechanical basis for chromosome function. Proc Natl Acad Sci *U S A* **101**:12592-12597.

670 **Knoll, A and Puchta, H.** (2011) The role of DNA helicases and their interaction partners in genome stability and meiotic recombination in plants J. Exp. Bot. **62**: 1565-1579.**Kolas, N.K., Svetlanov, A., Lenzi, M.L., Macaluso, F.P., Lipkin, S.M., Liskay, R.M., Greally, J., Edelmann, W., and Cohen, P.E.** (2005). Localization of MMR proteins on meiotic chromosomes in mice indicates distinct functions during prophase I. J Cell Biol **171**:447-458.

676 **Kunzel, G., Korzun, L., and Meister, A.** (2000). Cytologically integrated physical restriction fragment length polymorphism maps for the barley genome based on translocation breakpoints. Genetics **154**:397-412.

679 **Kunzel, G., and Waugh, R.** (2002). Integration of microsatellite markers into the translocation-based physical RFLP map of barley chromosome 3H. Theor. Appl. Genet. **105**:660-665.

682 **Lipkin, S.M., Moens, P.B., Wang, V., Lenzi, M., Shanmugarajah, D., Gilgeous, A., Thomas, J., Cheng, J., Touchman, J.W., Green, E.D., et al,** (2002). Meiotic arrest and aneuploidy in MLH3-deficient mice. Nat. Gen. **31**:385-390.

685 **Lipkin, S.M., Wang, V., Jacoby, R., Banerjee-Basu, S., Baxevanis, A.D., Lynch, H.T., Elliott, R.M., and Collins, F.S.** (2000). MLH3: a DNA mismatch repair gene associated with mammalian microsatellite instability. Nat. Gen. **24**:27-35.

688 **Lundqvist, U., Franckowiak, J.D., and Konishi, T.** (1997). New and revised descriptions
689 of barley genes. Barley Genet. Newsl. **26**:22-516.
690 **Luo, Q., Li, Y.F., Shen, Y., and Cheng, Z.K.** (2014). Ten Years of Gene Discovery for
691 Meiotic Event Control in Rice. J Genet Genomics **41:**125-137.
692 **Macgregor, H.C.** (2012) So what's so special about these things called lampbrush
693 chromosomes? Chromosome Research **20**: 903 – 904
694 **Matos, J. and West, S.C.** (2014) Holliday junction resolution: Regulation in space and time.
695 DNA Repair 19:176–181
696 **Martinez-Perez, E.** (2009). Meiosis in cereal crops: the grasses are back. Genome Dyn **5**:26-
697 42.
698 **Mercier, R., Jolivet, S., Vezon, D., Huppe, E., Chelysheva, L., Giovanni, M., Nogue, F.,**
699 **Doutriaux, M.P., Horlow, C., Grelon, M., et al,** (2005). Two meiotic crossover
700 classes cohabit in Arabidopsis: one is dependent on MER3,whereas the other one is
701 not. Curr Biol **15**:692-701.
702 **Mercier, R., Mezard, C., Jenczewski, E., Macaisne, N., and Grelon, M.** (2014). The
703 Molecular Biology of Meiosis in Plants. Annu. Rev. Plant Biol. **66**:5.1–5.31.
704 **Metzler-Guillemain, C., and de Massy, B.** (2000). Identification and characterization of an
705 SPO11 homolog in the mouse. Chromosoma **109**:133-138.
706 **Nakagawa, T., and Kolodner, R.D.** (2002). The MER3 DNA helicase catalyzes the
707 unwinding of Holliday junctions. J. Biol. Chem. **277**:28019-28024.
708 **Nicolette, M.L., Lee, K., Guo, Z., Rani, M., Chow, J.M., Lee, S.E., and Paull, T.T.** (2010)
709 Mre11-Rad50-Xrs2 and Sae2 promote 5' strand resection of DNA double-strand
710 breaks. Nat Struct Mol Biol. 17(12):1478-85
711 **Nilsson, N.O., Sall, T., and Bengtsson, B.O.** (1993). Chiasma and Recombination Data in
712 Plants - Are They Compatible. Trends in Genetics **9**:344-348.
713 **Nishant, K.T., Plys, A.J., and Alani, E.** (2008). A mutation in the putative MLH3
714 endonuclease domain confers a defect in both mismatch repair and meiosis in
715 Saccharomyces cerevisiae. Genetics **179**:747-755.
716 **Novak, J.E., Ross-Macdonald, P.B., and Roeder, G.S.** (2001). The budding yeast Msh4
717 protein functions in chromosome synapsis and the regulation of crossover
718 distribution. Genetics **158**:1013-1025.
719 **Phillips, D., Nibau, C., Wnetrzak, J., and Jenkins, G. (**2012). High Resolution Analysis of
720 Meiotic Chromosome Structure and Behaviour in Barley (Hordeum vulgare L.). Plos
721 One **7**(6): e39539. doi:10.1371/journal.pone.0039539.

Phillips, D., Wnetrzak, J., Nibau, C., Barakate, A., Ramsay, L., Wright, F., Higgins, J.D., Perry, R.M., and Jenkins, G. (2013). Quantitative high resolution mapping of HvMLH3 foci in barley pachytene nuclei reveals a strong distal bias and weak interference. J. Exp. Bot. **64**:2139-2154.

Ramsay, L., Colas, I., and Waugh, R. (2014). Modulation of Meiotic Recombination. J. Kumlehn, N. Stein (eds.), Biotechnological Approaches to Barley Improvement, Biotechnology in Agriculture and Forestry **69**, DOI 10.1007/978-3-662-44406-1_16

Ranjha, L., Anand, R., and Cejka, P. (2014). The Saccharomyces cerevisiae Mlh1-Mlh3 heterodimer is an endonuclease that preferentially binds to Holliday junctions. J Biol Chem **289**:5674-5686.

Raynard, S., Niu, H., and Sung, P. (2008) DNA double-strand break processing: the beginning of the end. Genes Dev. 2008 Nov 1; 22(21): 2903–2907.

Riley, R., Law, C.N., and Chapman, V. (1981). The Control of Recombination. Philos T Roy Soc B **292**:529-534.

Roesner, L.M., Mielke, C., Faehnrich, S., Merkhoffer, Y., Dittmar, K.E., Drexler, H.G., and Dirks, W.G. (2014). Localization of MLH3 at the centrosomes. Int. J. Mol. Sci. **15**:13932-13937.

Roesner, L.M., Mielke, C., Fahnrich, S., Merkhoffer, Y., Dittmar, K.E.J., Drexler, H.G., and Dirks, W.G. (2013). Stable Expression of MutL gamma in Human Cells Reveals No Specific Response to Mismatched DNA, But Distinct Recruitment to Damage Sites. J Cell Biochem **114**:2405-2414.

Rogacheva, M.V., Manhart, C.M., Chen, C., Guarne, A., Surtees, J., and Alani, E. (2014). Mlh1-Mlh3, a meiotic crossover and DNA mismatch repair factor, is a Msh2-Msh3-stimulated endonuclease. J Biol Chem **289**:5664-5673.

Salomé, P.A., Bomblies, K., Fitz J., Laitinen, R.A.E., Warthmann, N., Yant, L., and Weigel, D. (2011) The recombination landscape in Arabidopsis thaliana F2 populations. Heredity 108(4):447-455.

Santos, J.L. (1999) The relationship between synapsis and recombination: two different views. Heredity 82(1): 1–6

Schindelin, J., Arganda-Carreras, I., Frise, E., Kaynig, V., Longair, M., Pietzsch, T., Preibisch, S., Rueden, C., Saalfeld, S., Schmid, B., et al, (2012). Fiji: an open-source platform for biological-image analysis. Nat. Meth. **9**:676-682.

Shinohara, A., Gasior, S., Ogawa, T., Kleckner, N., and Bishop, D.K. (1997). Saccharomyces cerevisiae recA homologues RAD51 and DMC1 have both distinct and overlapping roles in meiotic recombination. Genes to Cells **2**:615-629.

Snowden, T., Acharya, S., Butz, C., Berardini, M., and Fishel, R. (2004). hMSH4-hMSH5 recognizes Holliday junctions and forms a meiosis-specific sliding clamp that embraces homologous chromosomes. Molecular Cell **15**:437-451.

Stacey, N.J., Kuromori, T., Azumi, Y., Roberts, G., Breuer, C., Wada, T., Maxwell, A., Roberts, K., and Sugimoto-Shirasu, K. (2006). Arabidopsis SPO11-2 functions with SPO11-1 in meiotic recombination. Plant J **48**:206-216.

Stack, S.M., and Anderson, L.K. (2001). A model for chromosome structure during the mitotic and meiotic cell cycles. Chromosome Res **9**:175-198.

Storlazzi, A., Gargano, S., Ruprich-Robert, G., Falque, M., David, M., Kleckner, N., and Zickler, D. (2010). Recombination Proteins Mediate Meiotic Spatial Chromosome Organization and Pairing. Cell **141**:94-106.

Svetlanov, A., Baudat, F., Cohen, P.E., and de Massy, B. (2008). Distinct functions of MLH3 at recombination hot spots in the mouse. Genetics **178**:1937-1945.

Thacker, D., Mohibullah, N., Zhu, X., and Keeney, S. (2014). Homologue engagement controls meiotic DNA break number and distribution. Nature **510**:241-246.

Vonesch, C., and Unser, M. (2008). A fast thresholded landweber algorithm for wavelet-regularized multidimensional deconvolution. Ieee T Image Process **17**:539-549.

Wang, M., Wang, K., Tang, D., Wei, C., Li, M., Shen, Y., Chi, Z., Gu, M., and Cheng, Z. (2010). The central element protein ZEP1 of the synaptonemal complex regulates the number of crossovers during meiosis in rice. Plant Cell **22**:417-430.

Wang, T.F., and Kung, W.M. (2002). Supercomplex formation between Mlh1-Mlh3 and Sgs1-Top3 heterocomplexes in meiotic yeast cells. Biochem. Biophys. Res. Commun. **296**:949-953.

Zakharyevich, K., Ma, Y., Tang, S., Hwang, P.Y., Boiteux, S., Hunter, N. (2010). Temporally and biochemically distinct activities of Exo1 during meiosis: double-strand break resection and resolution of double Holliday junctions. Mol Cell.; **40**:1001–1015.

Zhang, L.R., Wang, S.X., Yin, S., Hong, S., Kim, K.P., and Kleckner, N. (2014). Topoisomerase II mediates meiotic crossover interference. Nature **511**:551-556.

Zickler, D. (2006). From early homologue recognition to synaptonemal complex formation. Chromosoma **115**:158-174.

FIGURE LEGENDS

Figure 1: *des10* mapping.

des10 exhibits a semi-sterile phenotype (**a**) producing fewer seeds per ear (7.0±2.7) in *des10* than wild-type (13.7±3.7). The *des10* region (**b**) was initially delineated between two SNP markers (11_11273 and 11_21203) on the long arm of chromosome 5H and then fine mapped on an extended F_2 population to a 0.2cM region between two markers (MLOC_17896 and MLOC_34818) located on the same BAC contig (contig_38588). The only exonic polymorphism for the genes within this BAC contig was a deletion in MLOC_52425 encoding the barley ortholog of *HvMLH3*.

Figure 2: *des10* mutation.

(a) Alignment of *HvMlh3* gene sequences in wt and *des10*, with exons are highlighted in grey. The 159bp deletion removes the entire 17th exon coding for the peptide sequence HAADERIRLEELRSK without affecting reading frame. **(b)** The Histidine kinase-like ATPases and the MutL_Trans domains are unaffected but the *des10* Mutl-C domain is missing the majority of the metal binding motif QHAADERIRLEE (red box). This 15 amino acid deletion potentially affects the Mutl-C conformation in *des10* **(c)** as compared to the wild-type **(d).**

Figure 3: Reduced chiasmata and abnormal chromosome segregation in *des10*.

3D confocal optical section of wild-type **(a-d)** and *des10* **(e-h)** meiocytes (Scale bars 10 µm). At pachytene, homologous chromosomes are paired in both wild-type **(a)** and *des10* **(e)** as shown with the 45s (red) and 5s (green) probes. wild-type metaphase I **(b)** has seven ring bivalents that can be identified with 45S (red) and 5S (green) probes, whereas *des10* metaphase I **(f)** averages 9.2 chiasmata per nucleus with occasional univalents. During anaphase I, chromosomes segregate to each pole in wild-type **(c)** while chromosome mis-segregation is evident in *des10* **(g)**. Tetrad are normal and genetically balanced in wt **(d)** but not in *des10* **(h)** showing **(i)** Histogram of the distribution of chiasmata per cell for *des10* and wild-type and **(j)** a table of the number of chiasmata per chromosome in wild-type and *des10.*

Figure 4: Genetic mapping in F_3 families.

Alignment of the physical sequence (in Mbp) with consensus genetic map (in cM) for chromosome 1H with comparisons to the genetic maps calculated from BW230 (*des10)* x Morex F_3 families derived from F_2 individuals homozygous for either the wild-type or *des10* mutant allele at *HvMlh3*. Estimated centromere position on genetic map marked in red.

Figure 5: Comparison of synapsis in wild-type and *des10*.

Progression of synapsis in wild-type and *des10* demonstrated by the immuno-localization of AtASY1 (green) and AtZYP1 (magenta) on formaldehyde fixed meiocytes. Cells visualised by 3D-SIM show the progression of synapsis in wild-type **(a-f)** and *des10* **(g-l)** at leptotene **(a,b,g,h),** zygotene **(c,d,i,j)** and pachytene **(e,f,k,l)** together with detailed views of white squared regions (squares in **a,c,e,g,i,k**) shown in **(b,d,f,h,j,l).** Scale bars 5µm

Figure 6: Imaris modelling of *des10* pachytene like cell.

a) 3D view from Imaris of *des10* cell from Figure 5k with ASY1 labelling. **b**) Individual bivalent labelling in different colours using Imaris tracking. **c**) the distance between the two homologous chromosomes is 0.1µm corresponding to the wt SC distance.

Figure 7: EDU time course in wt and *des10.*

Percentage of cells in each meiotic stage category and 3D confocal optical sections of wild-type and *des10* meiocytes at 6h (**a-c**), 18h (**d,f**), 24h (**g-i**), 48h (**j-l**) and 68h (**m-o**). Scale bars 5µm. PM, TB, Lept, Zyg, Pach, Dip, MI, AI signifying Pre-meiotic, Telomere bouquet, Leptotene, Zygotene, Pachytene, Diplotene, Metaphase I and Anaphase I respectively.

Figure 8: Distribution of ZYP1 and HvMLH3 during prophase.

Wild-type (**a-l**) and *des10* (**m-x**) meiotic progression monitored using antibodies raised against HvZYP1 (magenta) and HvMLH3 (green) using 3D-SIM with detailed views of white squared regions (squares in **c,g,k,o,s,w** shown in **d,h,l,p,t,x**). At early zygotene in both wild-type (**a-d**) and *des10* (**m-p**) MLH3 signal is abundant (**b,n**) in the nucleus including associations with the chromosomes axes (**d,p**). This continues into early pachytene, in both wild-type (**e-h**) and *des10* (**q-t**). However, in the wild-type (**g,h**) a few foci with a stronger signal potentially marking the finalized COs become evident (triangles) while it is difficult to differentiate foci in *des10* (**s,t).** At late pachytene (**i-l, u-x**), CO foci (triangles) are seen

clearly in wild-type as compared to weaker un-associated signals (circle) (**k,l**). Weaker SC associated foci (**w-x**) are discernible in *des10* (triangles) though considerable MLH3 signal remains in the nucleus and on the axes. Scale bars 5µm

Table 1: Recombination foci in wild-type and *des10*.

Table showing the number of AtDMC1, AtRAD51 and AtMSH4 foci in wild-type and *des10* at the telomere bouquet, the stage of de-clustering of the telomere and the linear ASY1 stage.

Stage	**Protein**	**WT**	***des10***	**TTEST static**
Telomere bouquet	RAD51	127.27 ±55.38	142.2 ±49.3	2.46E-01
De-clustering	RAD51	164.96 ±63.12	240.8 ±80.6	6.48E-04
Linear ASY1	RAD51	349.3 ±79.5	700.3 ±128.2	1.721E-05
	DMC1	361.3 ±62.9	766.8 ±147.3	4.4873E-06
	MSH4	323.2 ±33.4	639.5 ±79.5	3.53682E-06

SUPPORTING INFORMATION

Figure S1: *des10* cDNA and polymorphism.

PCR-sequencing of MLOC_52425 (*HvMLH3*) revealed a single polymorphism between *des10* and wild-type lines including Bowman and the original mutant background cultivar Betzes **(a)**, due to a 159bp deletion potentially removing the 17th exon. Sequencing amplified cDNA from anthers and young inflorescence in both wild-type and *des10* confirmed that the mutant cDNA was missing the 17th exon, leaving the sequence in frame **(b)**.

Figure S2: Recombination in F_3 families for chromosomes 2H-7H.

Comparison of the consensus genetic maps (a) for chromosomes 2H-7H with those calculated from BW230 (*des10)* x Morex F_3 families derived from F_2 individuals homozygous for either the wild-type (b) or *des10* mutant allele at *HvMlh3* (c). The position of the centromere is marked in red on all consensus maps and the position of *des10* marked in red on the 5H consensus map.

Figure S3: Recombination in F3 families at three intervals.

KASP markers were designed to SNPs delineating intervals (box) in three contrasting genomic regions (centromeric 4H, distal 6HS and distal 7HL) **(a).** Recombination in the three unlinked genetic intervals is reduced by 61% in individuals in F_3 families derived from F_2 individuals homozygous for the *des10 HvMlh3* allele compared to those derived from individuals homozygous for the wild-type allele **(b).**

Figure S4: Synapsis details in wild-type and *des10*.

Detailed progression of synapsis in wild-type **(a-l)** *and des10* (**m-x**) cells demonstrated by the immuno-localization of AtASY1 (green) and AtZYP1 (magenta) on formaldehyde fixed meiocytes. Cells visualised by 3D-SIM show the progression of synapsis in wild-type at leptotene (**a-d**), zygotene (**e-h**), and pachytene (**i-l**) together with detailed views of white squared regions compare to the progression of synapsis in *des10* at leptotene (**m-p**), zygotene (**q-t**), and pachytene (u-x) together with detailed views of white squared regions. Scale bars 5µm.

Figure S5: Comparison of Confocal and Structured Illumination Microscopy images.

Confocal images of (**a**) wild-type and (**b**) *des10* show a linear HvZYP1 (magenta) signal at pachytene and it is possible to count the number of HvMLH3 (green) foci in wild-type on the newly formed SC. The same cells imaged by 3D-SIM show that in wild-type (**c**), ZYP1 is indeed linear along the chromosome. In *des10* (**d**), ZYP1 signal is seen along the entire length of the chromosome suggesting that pachytene is achieved but the signal remains non-continuous, suggesting that ZYP1 loading is not complete.

Figure S6: Meiocyte size.

The sizes of the nucleus were estimated using chromatin stain diameter (µm) at different stages of meiosis **(a)** gauged by ASY1 and ZYP1 labelling. Results show a lack of synchronicity between cell size and meiotic stage in *des10* relative to wild-type **(b).**

Figure S7: HvMLH3 foci count in wild-type late pachytene.

(**a**) 3D confocal image of wild-type pachytene labelled with HvZYP1 (magenta) and HvMLH3 (green) with the nucleus showing 21 MLH3 foci on the ZYP1 axes. (**b**) 3D SIM image gallery of wild-type pachytene labelled with HvZYP1 (magenta) and HvMLH3 (green) with numbering highlighting the foci presumably marking crossovers. This nucleus shows 18 MLH3 foci on the ZYP1 axes.

Figure S8: HvMLH3 foci in *des10*.

(**a**) 3D confocal image of a *des10* cell labelled with HvZYP1 (magenta) and HvMLH3 (green). This cell appears to be at pachytene as the ZYP1 signal is quite linear. Despite a high MLH3 background, 5 MLH3 foci can be seen associated with the ZYP1 axes. (**b**) 3D SIM image gallery of a *des10* cell labelled with HvZYP1 (magenta) and HvMLH3 (green) with the numbering highlighting the foci presumably marking crossovers. This nucleus shows 10 MLH3 foci on the ZYP1 axes although with 3D SIM the ZYP1 appears non-linear.

Figure S9: 3D localisation of RAD51.

AtRAD51 (green) protein initially loads onto the chromosome from the telomere region in both wild-type **(a)** and *des10* **(b).** As RAD51 protein signal moves from telomere to more proximal regions it becomes possible to count individual foci in wild-type **(c)** and *des10* **(d)**. Scale bars 5µm.

Figure S10: RAD51, DMC1 and MSH4 foci on SC spreads (squash).

Co- immunolocalization was also performed for (a) AtASY1 (green) and AtRAD51 (magenta), (b) AtASY1(green) and AtDMC1 (magenta), and (c) AtASY1 (green) and AtMSH4 (magenta), to monitor the localization of DSBs on the axial elements. In both wild-type and *des10* early (RAD51 and DMC1) and intermediate (MSH4) recombination proteins load on the chromosome axis (ASY1) revealing that crossing over intermediates are formed in both wild-type and *des10.* Scale bars 5µm.

Table S1: MLH3 foci counts.

Table showing the number of MLH3 foci at late pachytene in 3D stack images of wild-type and *des10 c*ells.

Figure 1: *des10* mapping.
des10 exhibits a semi-sterile phenotype (**a**) producing fewer seeds per ear (7.0±2.7) in *des10* than wild-type (13.7±3.7). The *des10* region (**b**) was initially delineated between two SNP markers (11_11273 and 11_21203) on the long arm of chromosome 5H and then fine mapped on an extended F_2 population to a 0.2cM region between two markers (MLOC_17896 and MLOC_34818) located on the same BAC contig (contig_38588). The only exonic polymorphism for the genes within this BAC contig was a deletion in MLOC_52425 encoding the barley ortholog of *HvMLH3*.

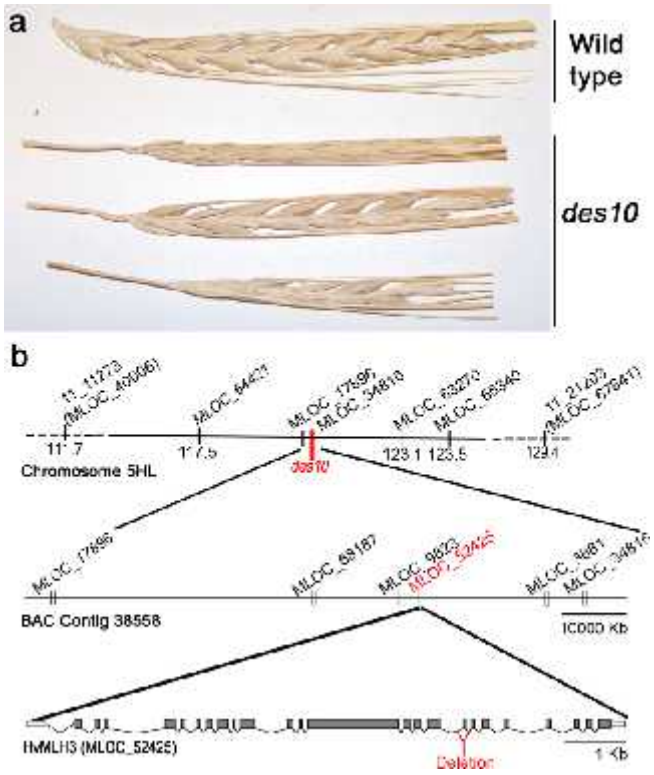

Figure 2: *des10* mutation.
(a) Alignment of *HvMlh3* gene sequences in wt and *des10*, with exons are highlighted in grey. The 159bp deletion removes the entire 17th exon coding for the peptide sequence HAADERIRLEELRSK without affecting reading frame. **(b)** The Histidine kinase-like ATPases and the MutL_Trans domains are unaffected but the *des10* Mutl-C domain is missing the majority of the metal binding motif QHAADERIRLEE (red box). This 15 amino acid deletion potentially affects the Mutl-C conformation in *des10* **(c)** as compared to the wild-type **(d).**

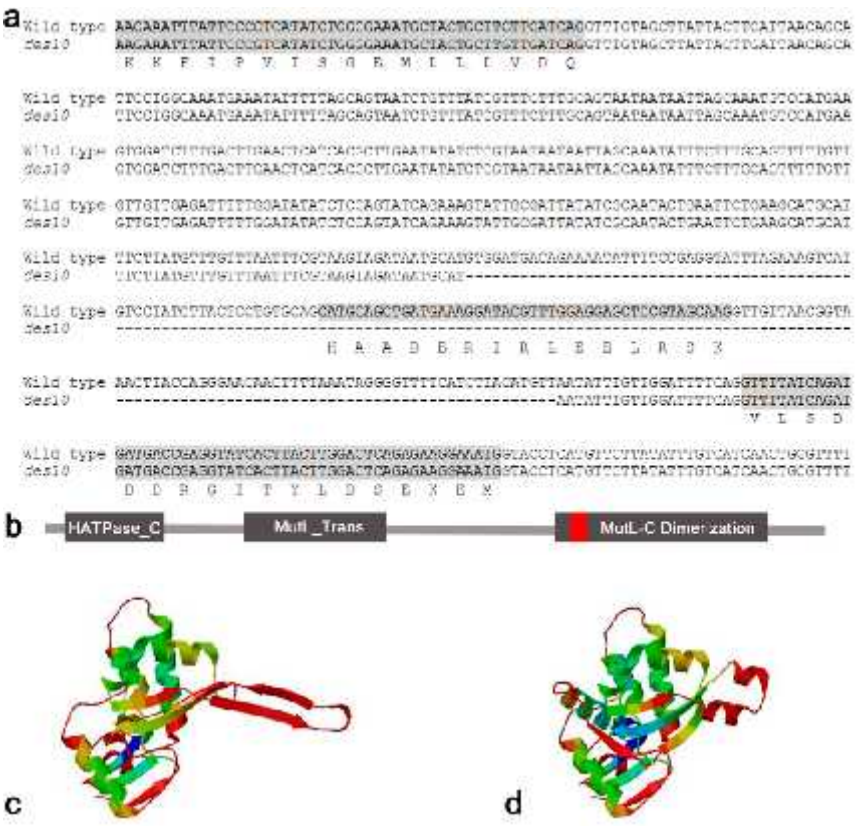

Figure 3: Reduced chiasmata and abnormal chromosome segregation in *des10.*
3D confocal optical section of wild-type **(a-d)** and *des10* **(e-h)** meiocytes (Scale bars 10 µm). At pachytene, homologous chromosomes are paired in both wild-type **(a)** and *des10* **(e)** as shown with the 45s (red) and 5s (green) probes. wild-type metaphase I **(b)** has seven ring bivalents that can be identified with 45S (red) and 5S (green) probes, whereas *des10* metaphase I **(f)** averages 9.2 chiasmata per nucleus with occasional univalents. During anaphase I, chromosomes segregate to each pole in wild-type **(c)** while chromosome mis-segregation is evident in *des10* **(g)**. Tetrad are normal and genetically balanced in wt **(d)** but not in *des10* **(h)** showing **(i)** Histogram of the distribution of chiasmata per cell for *des10* and wild-type and **(j)** a table of the number of chiasmata per chromosome in wild-type and *des10.*

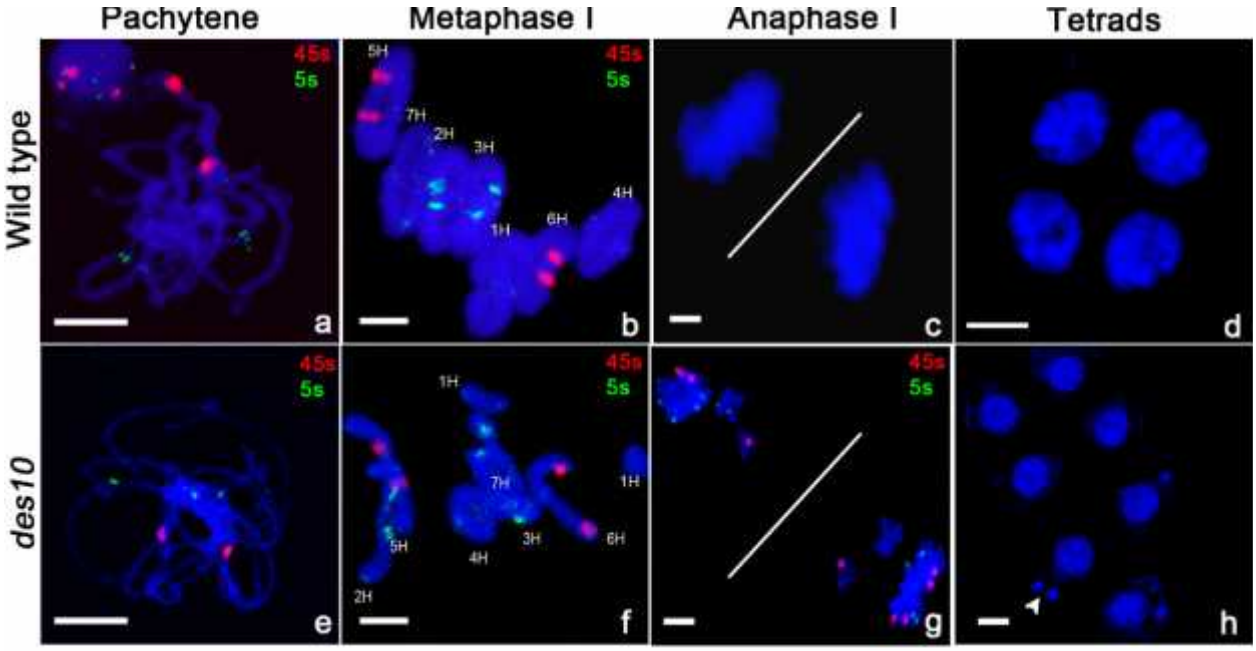

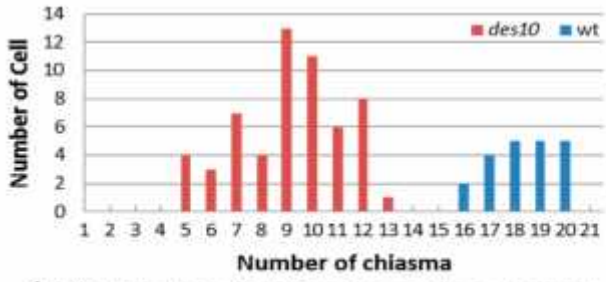

i- Distribution of chiasma number per cell

	1H	2H	3H	4H	5H	6H	7H	Total
wt	2.4	2.9	3.0	2.5	2.5	2.6	2.4	18.4
des10	1.1	1.3	1.3	1.4	0.9	1.0	1.2	9.2

j. Chiasma number per bivalent

Figure 4: Genetic mapping in F_3 families.
Alignment of the physical sequence (in Mbp) with consensus genetic map (in cM) for chromosome 1H with comparisons to the genetic maps calculated from BW230 (*des10)* x Morex F_3 families derived from F_2 individuals homozygous for either the wild-type or *des10* mutant allele at *HvMlh3*. Estimated centromere position on genetic map marked in red.

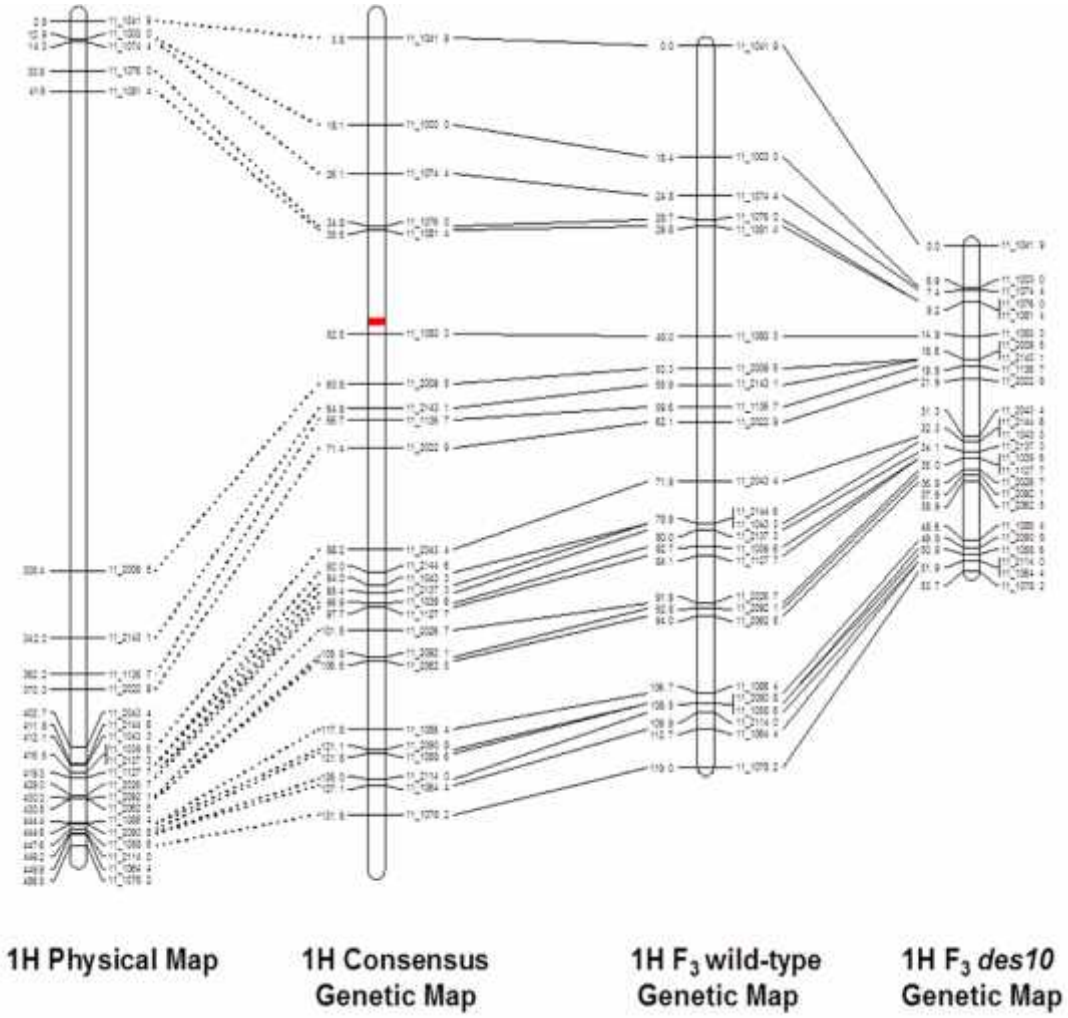

Figure 5: Comparison of synapsis in wild-type and *des10*.
Progression of synapsis in wild-type and *des10* demonstrated by the immuno-localization of AtASY1 (green) and AtZYP1 (magenta) on formaldehyde fixed meiocytes. Cells visualised by 3D-SIM show the progression of synapsis in wild-type **(a-f)** and *des10* **(g-l)** at leptotene **(a,b,g,h),** zygotene **(c,d,i,j)** and pachytene **(e,f,k,l)** together with detailed views of white squared regions (squares in **a,c,e,g,i,k**) shown in **(b,d,f,h,j,l).** Scale bars 5µm

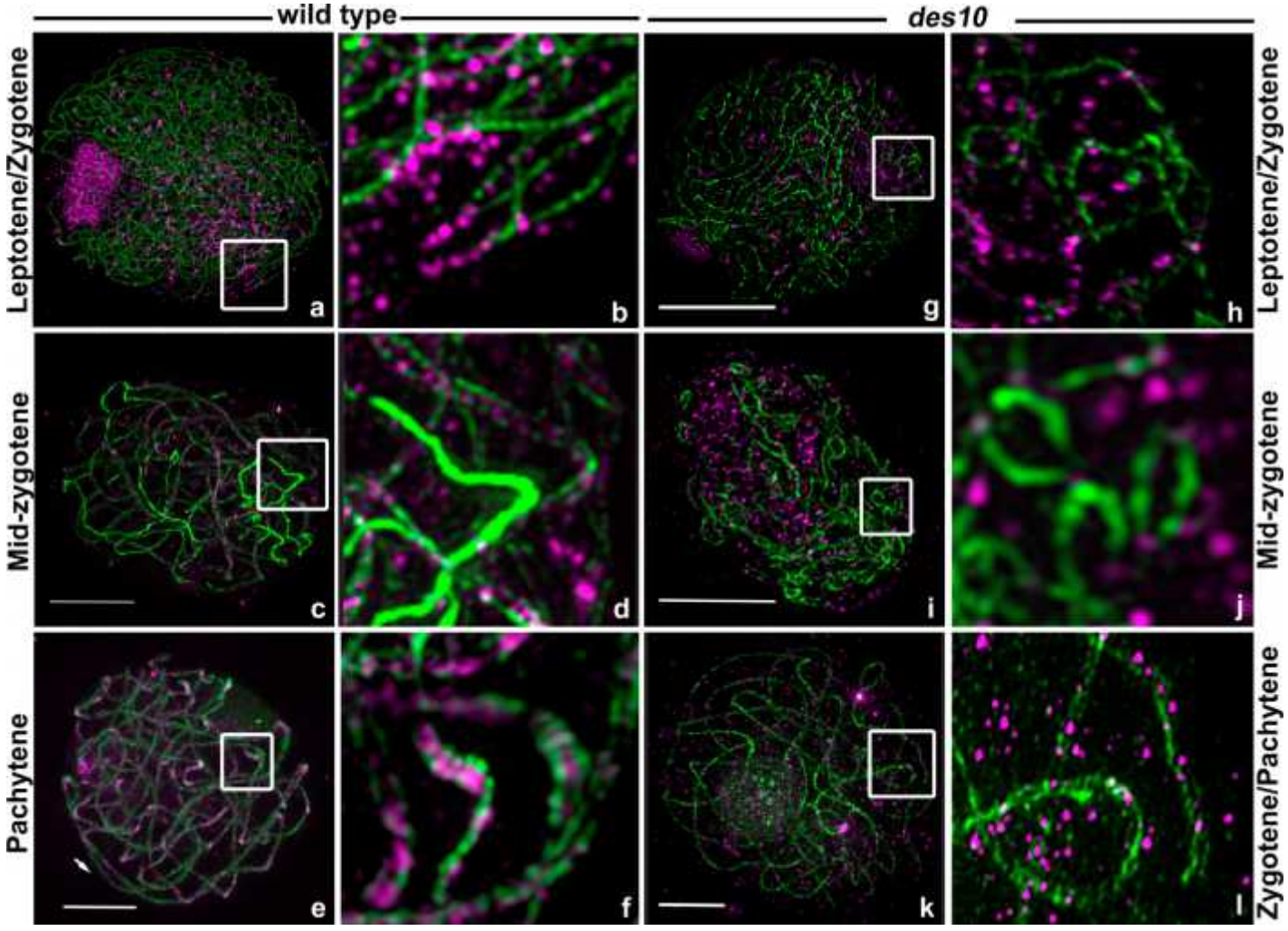

Figure 6: Imaris modelling of *des10* pachytene like cell.
a) 3D view from Imaris of *des10* cell from Figure 5k with ASY1 labelling. **b**) Individual bivalent labelling in different colours using Imaris tracking. **c**) the distance between the two homologous chromosomes is 0.1µm corresponding to the wt SC distance.

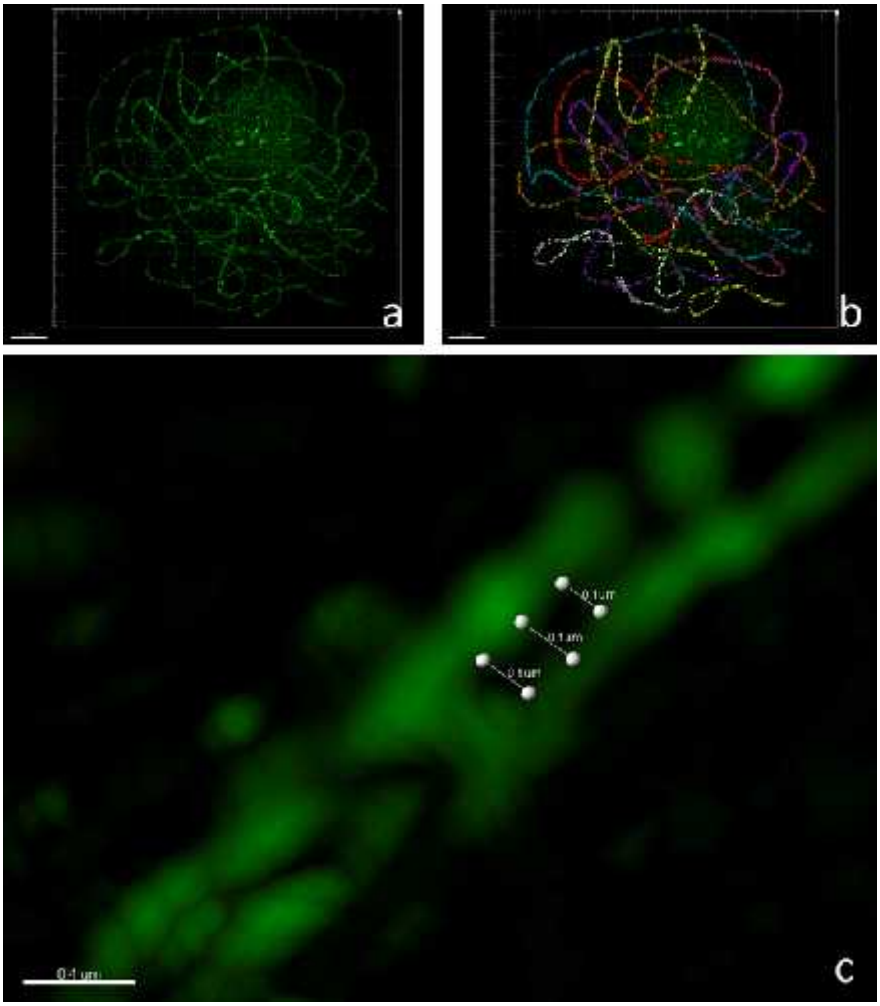

Figure 7: EDU time course in wt and *des10.*
Percentage of cells in each meiotic stage category and 3D confocal optical sections of wild-type and *des10* meiocytes at 6h (**a-c**), 18h (**d,f**), 24h (**g-i**), 48h (**j-l**) and 68h (**m-o**). Scale bars 5µm. PM, TB, Lept, Zyg, Pach, Dip, MI, AI signifying Pre-meiotic, Telomere bouquet, Leptotene, Zygotene, Pachytene, Diplotene, Metaphase I and Anaphase I respectively.

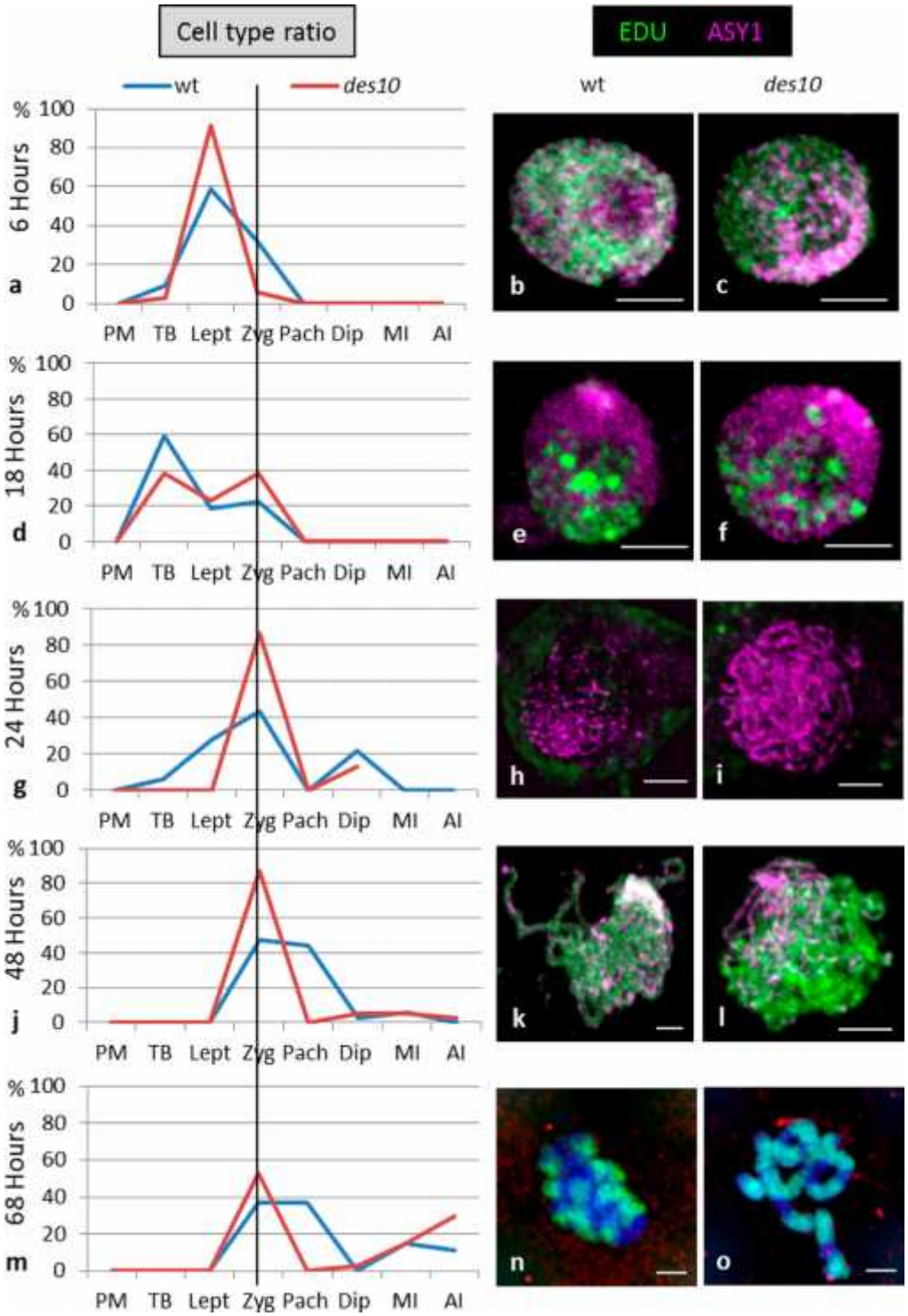

Figure 8: Distribution of ZYP1 and HvMLH3 during prophase.
Wild-type (**a-l**) and *des10* (**m-x**) meiotic progression monitored using antibodies raised against HvZYP1 (magenta) and HvMLH3 (green) using 3D-SIM with detailed views of white squared regions (squares in **c,g,k,o,s,w** shown in **d,h,l,p,t,x**). At early zygotene in both wild-type (**a-d**) and *des10* (**m-p**) MLH3 signal is abundant (**b,n**) in the nucleus including associations with the chromosomes axes (**d,p**). This continues into early pachytene, in both wild-type (**e-h**) and *des10* (**q-t**). However, in the wild-type (**g,h**) a few foci with a stronger signal potentially marking the finalized COs become evident (triangles) while it is difficult to differentiate foci in *des10* (**s,t**)**.** At late pachytene (**i-l, u-x**), CO foci (triangles) are seen clearly in wild-type as compared to weaker un-associated signals (circle) (**k,l**). Weaker SC associated foci (**w-x**) are discernible in *des10* (triangles) though considerable MLH3 signal remains in the nucleus and on the axes. Scale bars 5µm

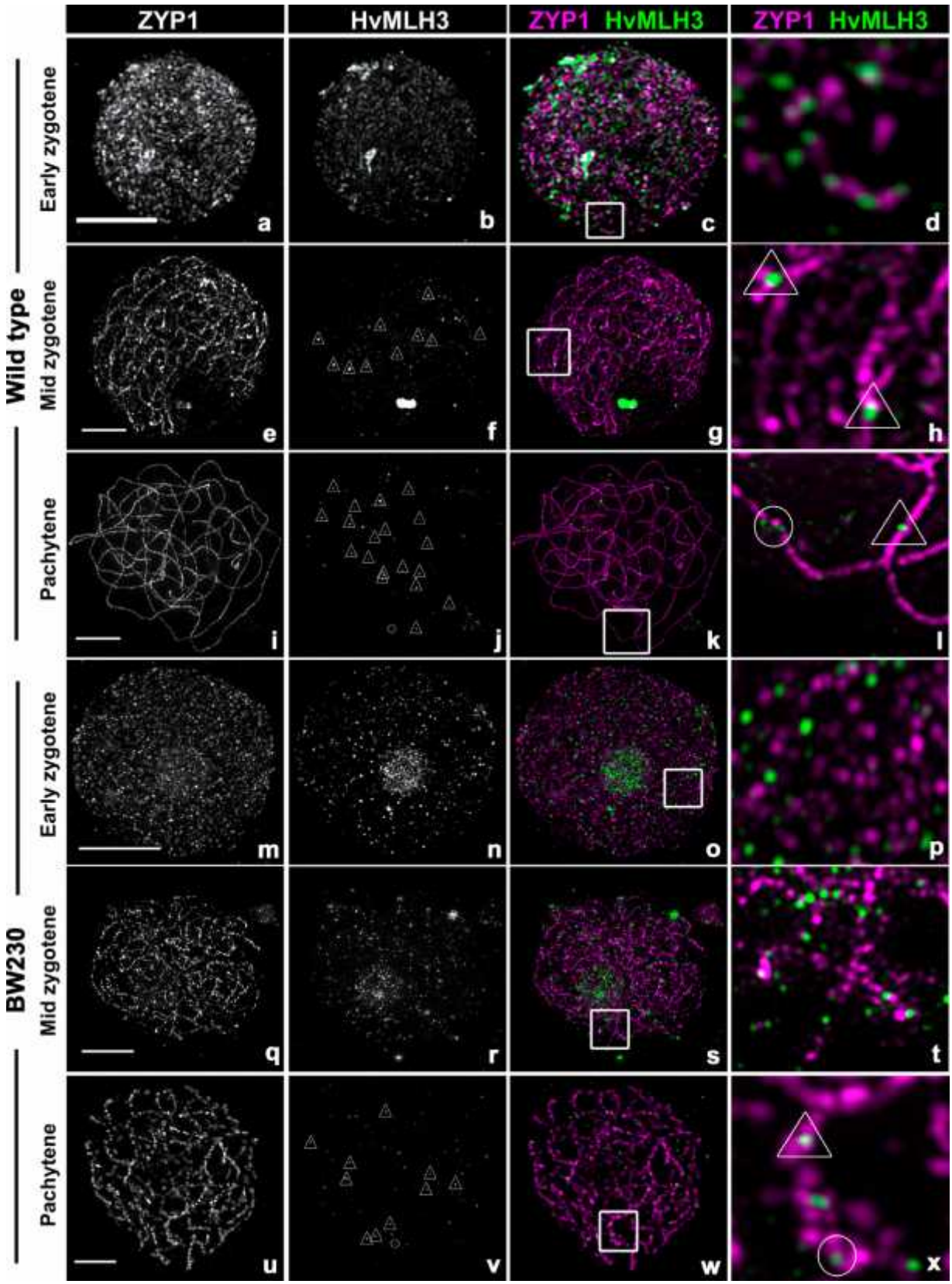
ZYP1
HvMLH3
ZYP1 HvMLH3
ZYP1 HvMLH3
Wild type
BW230
Early zygotene
Mid zygotene
Pachytene
Early zygotene
Mid zygotene
Pachytene
a
b
c
d
e
f
g
h
i
j
k
l
m
n
o
p
q
r
s
t
u
v
w
x

Table S1: MLH3 foci counts.

Table showing the number of MLH3 foci at late pachytene in 3D stack images of wild-type and *des10 c*ells.

wild-type Image no.	wild-type MLH3 foci	*des10* Image no.	*des10* MLH3 foci
Image 1	23	Image 1	7
Image 2	22	Image 2	7
Image 3	22	Image 3	6
Image 4	26	Image 4	7
Image 5	26	Image 5	9
Image 6	20	Image 6	7
Image 7	21	Image 7	6
Image 8	26	Image 8	9
Image 9	20	Image 9	6
Image 10	20	Image 10	7
Image 11	24	Image 11	8
Image 12	15	Image 12	6
Image 13	16	Image 13	10
Image 14	23	Image 14	4
Image 15	18	Image 15	6
Image 16	21	Image 16	8
Image 17	20	Image 17	12
Image 18	17	Image 18	8
Image 19	16	Image 19	9
		Image 20	9
		Image 21	6
		Image 22	8
		Image 23	8
		Image 24	9
		Image 25	8
		Image 26	7
		Image 27	8
		Image 28	8
		Image 29	9
		Image 30	10
Foci Total	**396**		**232**
Number of Cell	**19**		**30**
mean No./nucleus	**20.84**		**7.73**
SD	**3.40**		**1.60**

Figure S1: *des10* cDNA and polymorphism.
PCR-sequencing of MLOC_52425 (*HvMLH3*) revealed a single polymorphism between *des10* and wild-type lines including Bowman and the original mutant background cultivar Betzes **(a)**, due to a 159bp deletion potentially removing the 17th exon. Sequencing amplified cDNA from anthers and young inflorescence in both wild-type and *des10* confirmed that the mutant cDNA was missing the 17th exon, leaving the sequence in frame **(b)**.

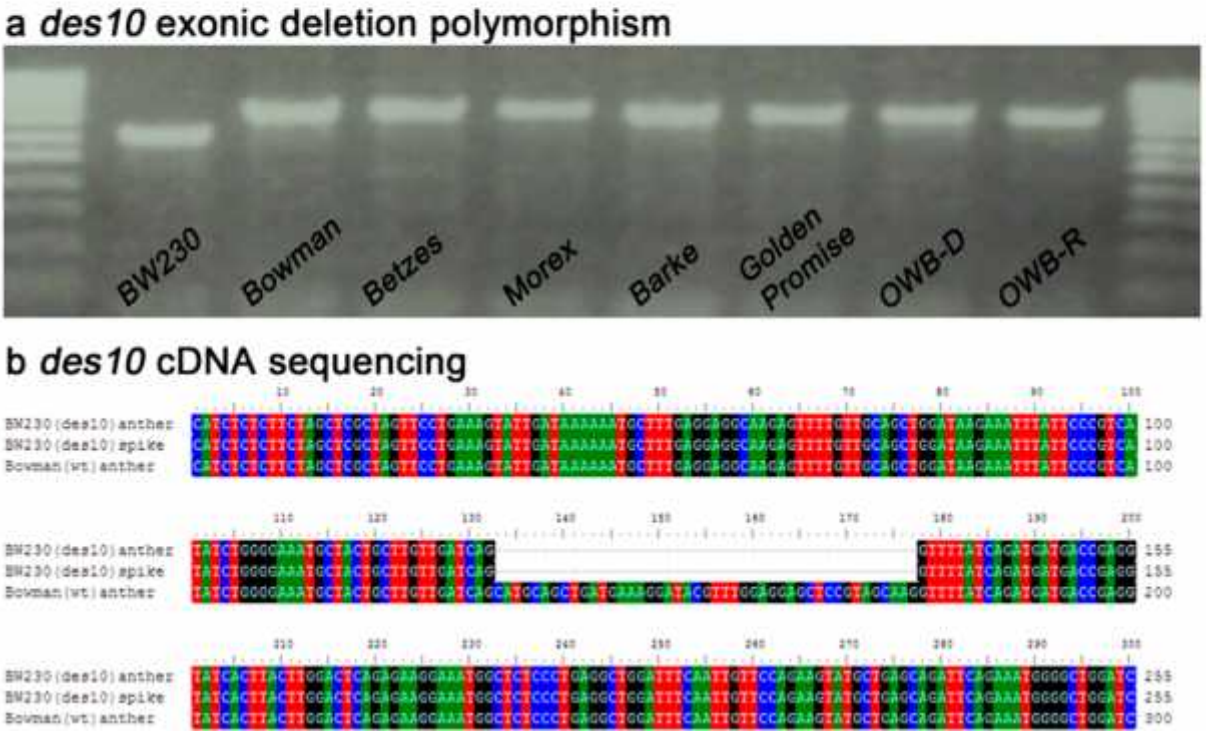

Figure S2: Recombination in F_3 families for chromosomes 2H-7H.
Comparison of the consensus genetic maps (a) for chromosomes 2H-7H with those calculated from BW230 (*des10)* x Morex F_3 families derived from F_2 individuals homozygous for either the wild-type (b) or *des10* mutant allele at *HvMlh3* (c). The position of the centromere is marked in red on all consensus maps and the position of *des10* marked in red on the 5H consensus map.

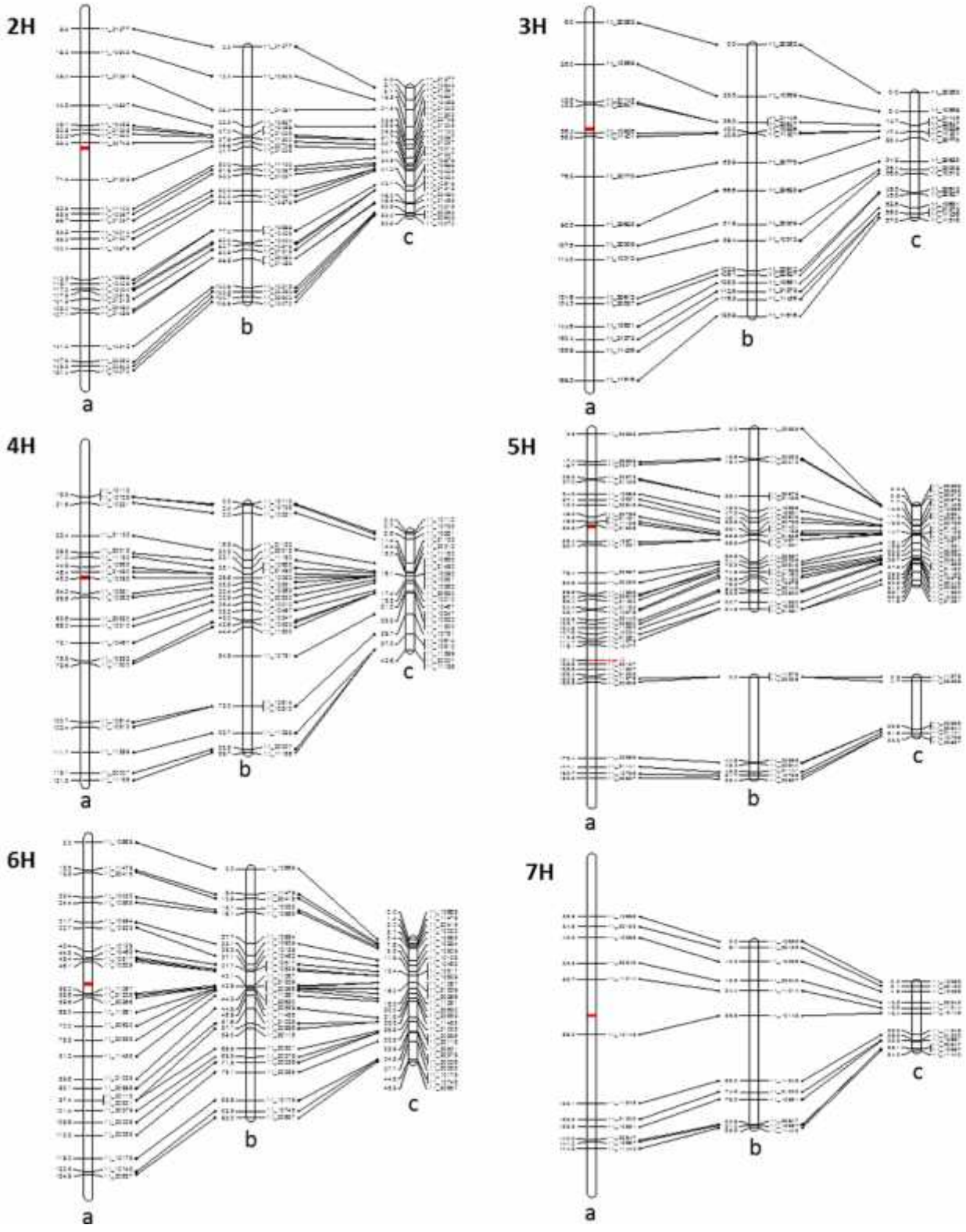

Figure S3: Effect on recombination in F_3 families.
KASP markers were designed to SNPs delineating intervals (box) in three contrasting genomic regions (centromeric 4H, distal 6HS and distal 7HL) **(a).** Recombination in the three unlinked genetic intervals is reduced by 61% in individuals in F_3 families derived from F_2 individuals homozygous for the *des10 HvMlh3* allele compared to those derived from individuals homozygous for the wild-type allele **(b).**

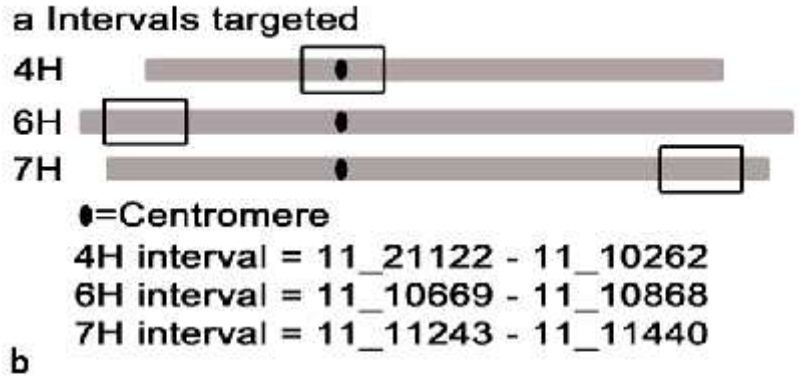

b

Interval	wt	*des10*	%
4H	0.184	0.100	55%
6H	0.380	0.099	26%
7H	0.412	0.150	36%
mean			39%

Figure S4: Synapsis details in wild-type and *des10*.
Detailed progression of synapsis in wild-type **(a-l)** *and des10* (**m-x**) cells demonstrated by the immuno-localization of AtASY1 (green) and AtZYP1 (magenta) on formaldehyde fixed meiocytes. Cells visualised by 3D-SIM show the progression of synapsis in wild-type at leptotene (**a-d**), zygotene (**e-h**), and pachytene (**i-l**) together with detailed views of white squared regions compare to the progression of synapsis in *des10* at leptotene (**m-p**), zygotene (**q-t**), and pachytene (u-x) together with detailed views of white squared regions. Scale bars 5µm.

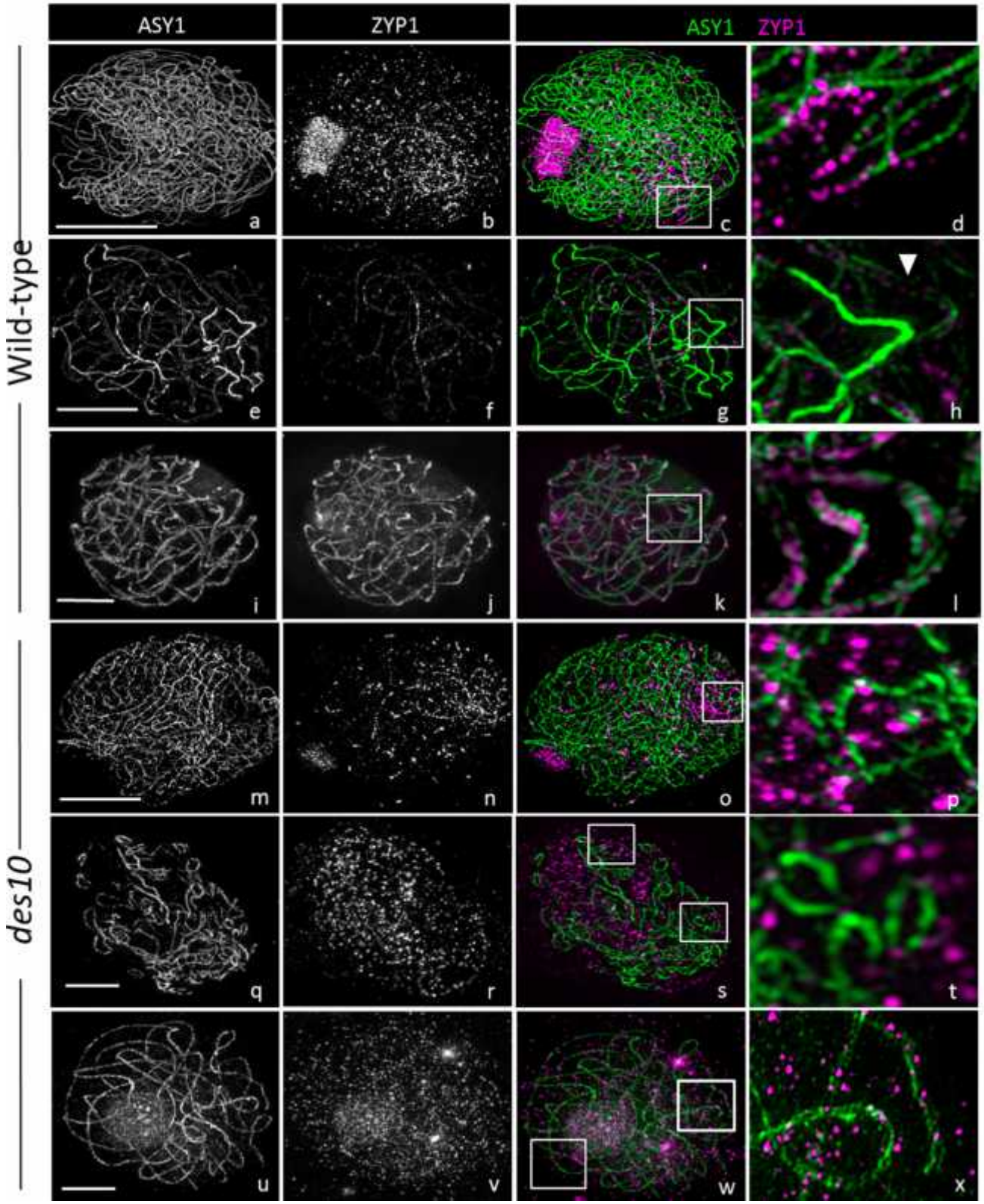

Figure S5: Comparison of Confocal and Structured Illumination Microscopy images.

Confocal images of (**a**) wild-type and (**b**) *des10* show a linear HvZYP1 (magenta) signal at pachytene and it is possible to count the number of HvMLH3 (green) foci in wild-type on the newly formed SC. The same cells imaged by 3D-SIM show that in wild-type (**c**), ZYP1 is indeed linear along the chromosome. In *des10* (**d**), ZYP1 signal is seen along the entire length of the chromosome suggesting that pachytene is achieved but the signal remains non-continuous, suggesting that ZYP1 loading is not complete.

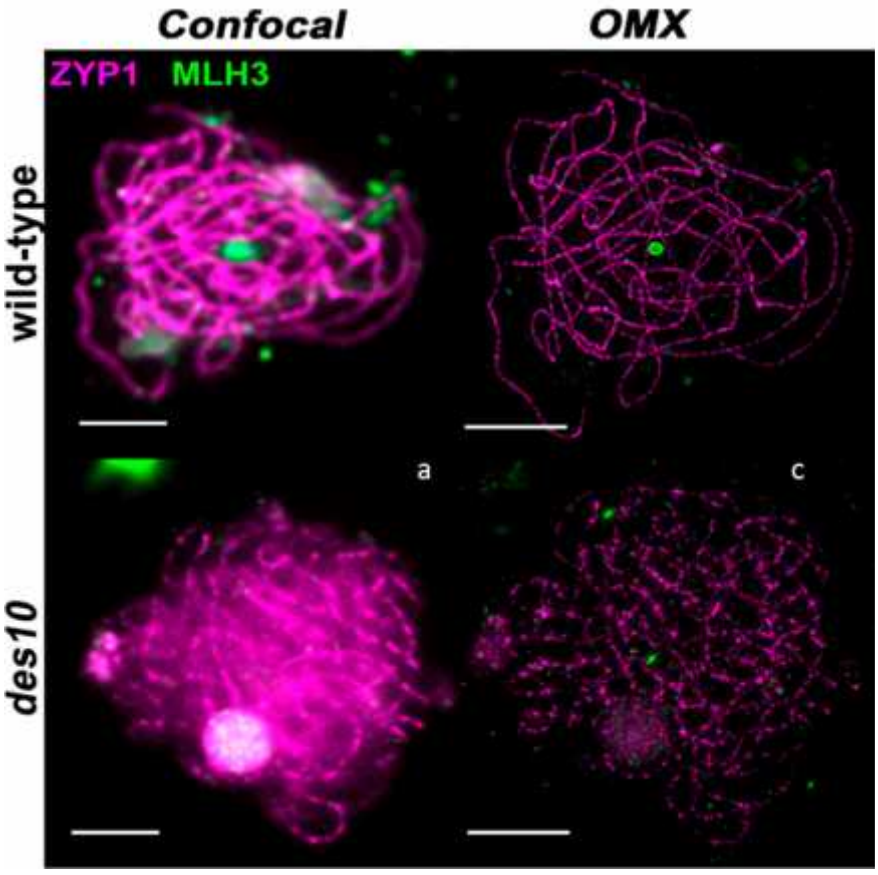

Figure S6: Meiocyte size.

The sizes of the nucleus were estimated using chromatin stain diameter (μm) at different stages of meiosis **(a)** gauged by ASY1 and ZYP1 labelling. Results show a lack of synchronicity between cell size and meiotic stage in *des10* relative to wild-type **(b)**.

a

	wild-type mean	*des10* mean
G2	11.19	11.91
Telomere bouquet	11.18	10.77
Leptotene/Zygotene	17.68	16.05
Mid zygotene	17.66	14.06
Early pachytene	17.23	13.90
Mid pachytene	15.73	18.14
Late pachytene	20.15	17.69
Diplotene	19.56	21.31

b

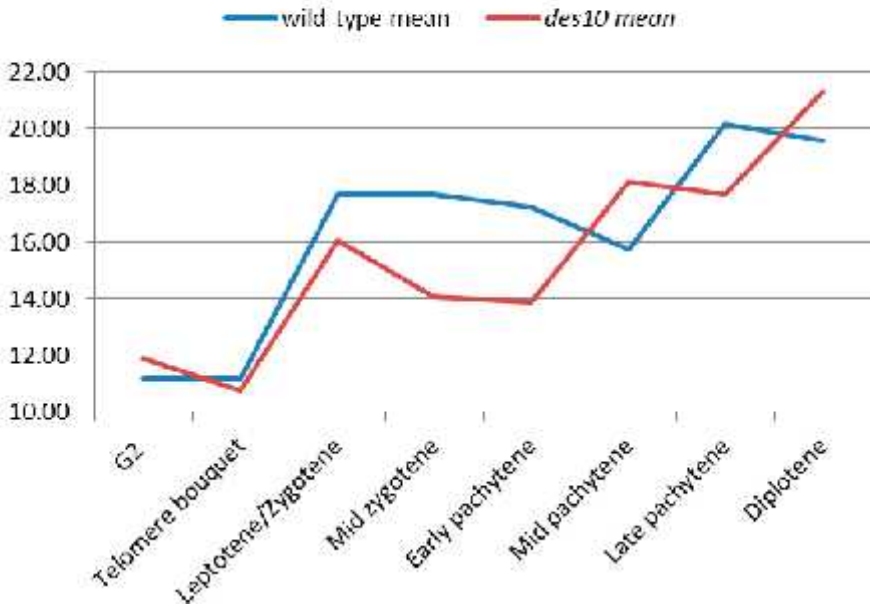

Figure S7: HvMLH3 foci count in wild-type late pachytene.
(**a**) 3D confocal image of wild-type pachytene labelled with HvZYP1 (magenta) and HvMLH3 (green) with the nucleus showing 21 MLH3 foci on the ZYP1 axes. (**b**) 3D SIM image gallery of wild-type pachytene labelled with HvZYP1 (magenta) and HvMLH3 (green) with numbering highlighting the foci presumably marking crossovers. This nucleus shows 18 MLH3 foci on the ZYP1 axes.

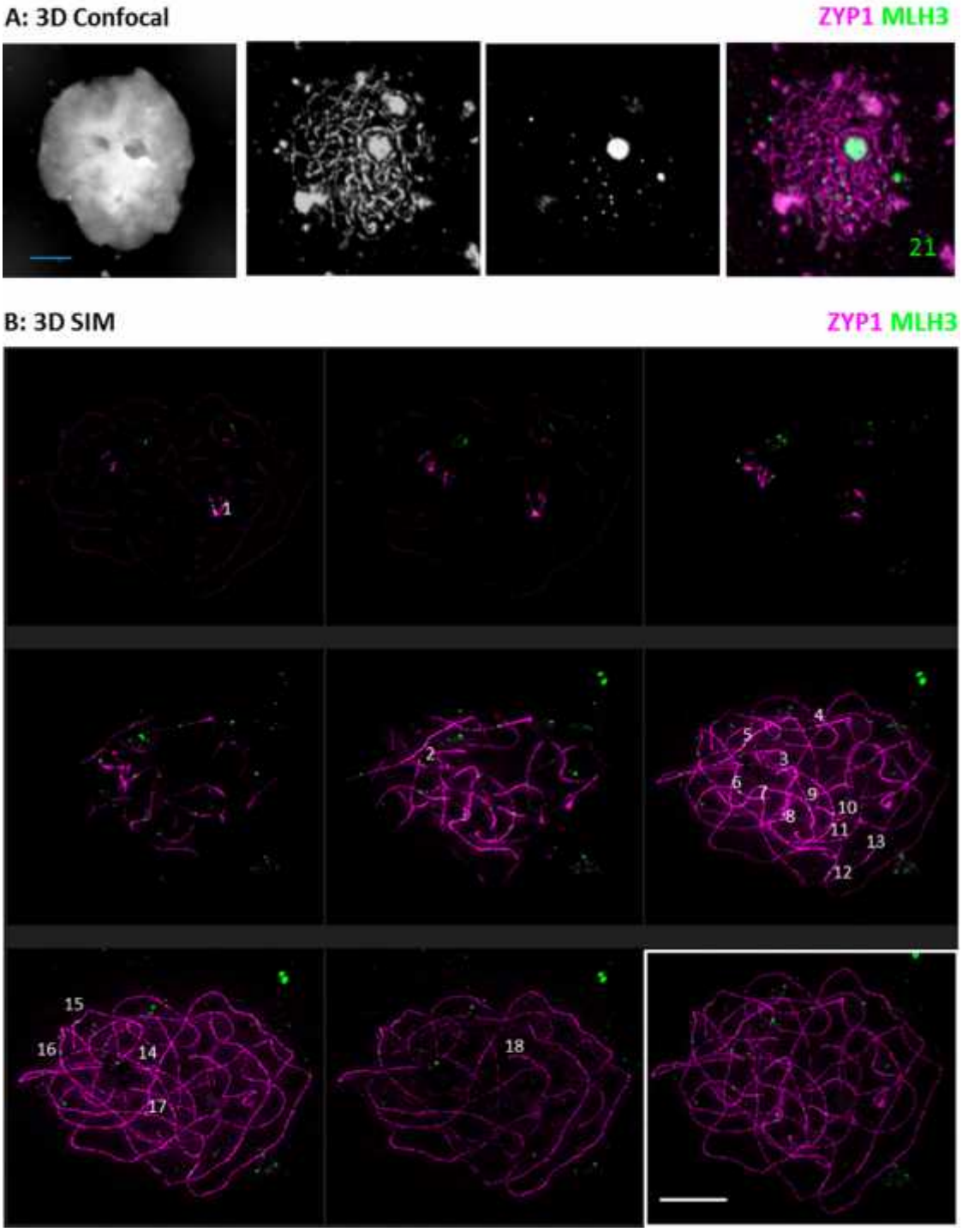

Figure S8: HvMLH3 foci in *des10*.
(**a**) 3D confocal image of a *des10* cell labelled with HvZYP1 (magenta) and HvMLH3 (green). This cell appears to be at pachytene as the ZYP1 signal is quite linear. Despite a high MLH3 background, 5 MLH3 foci can be seen associated with the ZYP1 axes. (**b**) 3D SIM image gallery of a *des10* cell labelled with HvZYP1 (magenta) and HvMLH3 (green) with the numbering highlighting the foci presumably marking crossovers. This nucleus shows 10 MLH3 foci on the ZYP1 axes although with 3D SIM the ZYP1 appears non-linear

A: Confocal ZYP1 MLH3

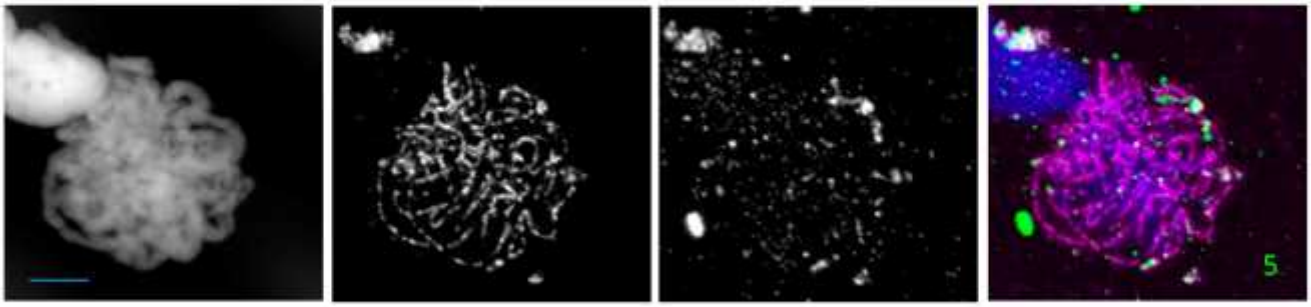

B: 3D SIM ZYP1 MLH3

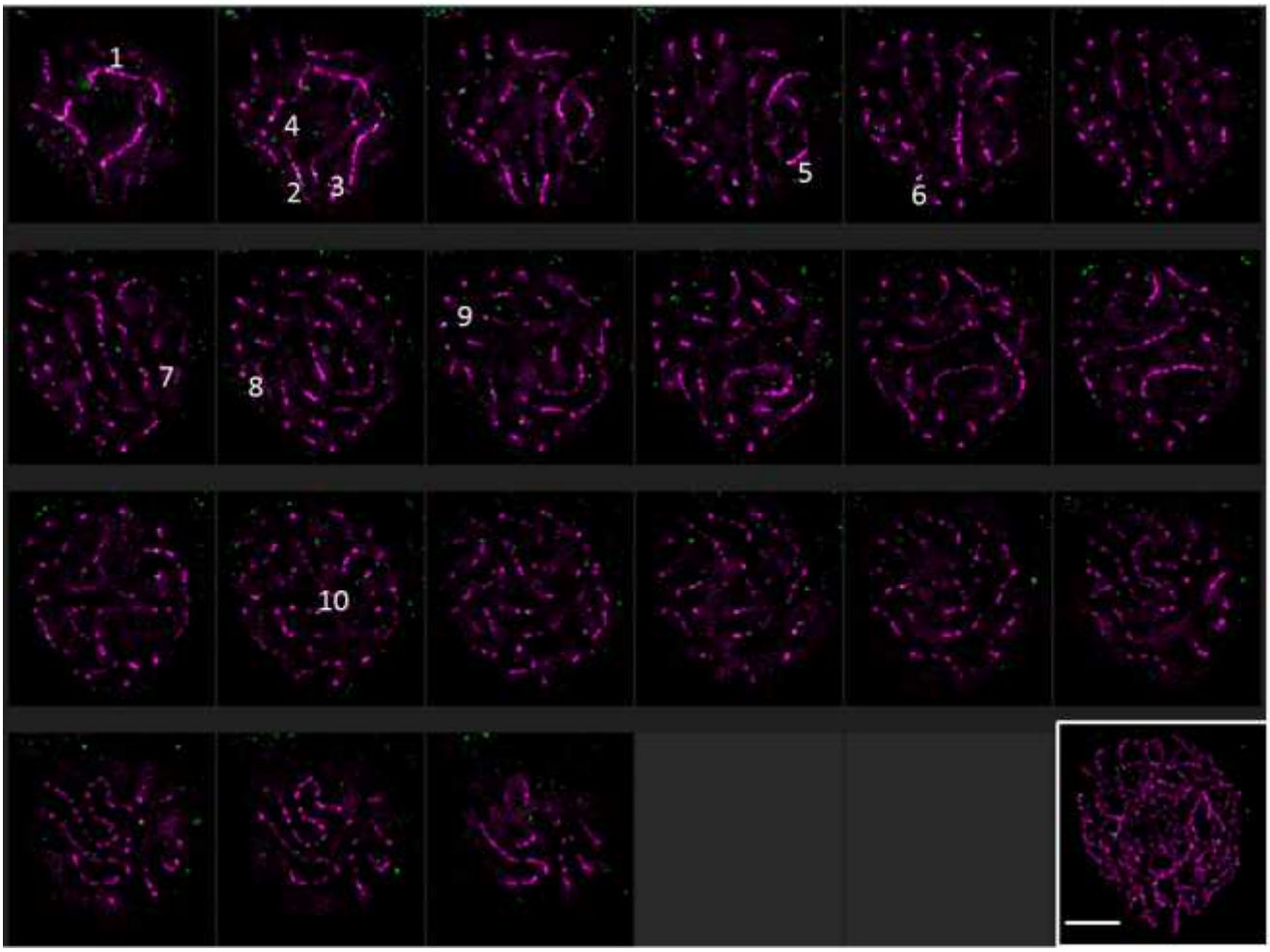

Figure S9: 3D localisation of RAD51.
AtRAD51 (green) protein initially loads onto the chromosome from the telomere region in both wild-type **(a)** and *des10* **(b).** As RAD51 protein signal moves from telomere to more proximal regions it becomes possible to count individual foci in wild-type **(c)** and *des10* **(d)**. Scale bars 5µm.

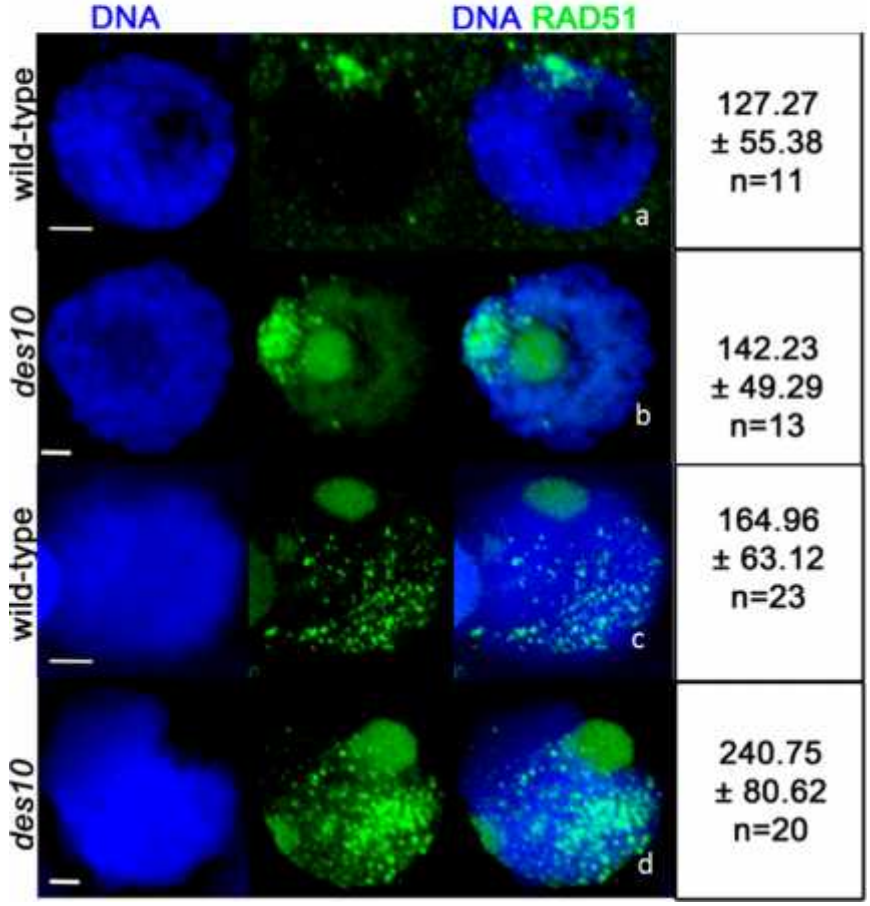

Figure S10: RAD51, DMC1 and MSH4 foci on SC spreads (squash).
Co- immunolocalization was also performed for (a) AtASY1 (green) and AtRAD51 (magenta), (b) AtASY1(green) and AtDMC1 (magenta), and (c) AtASY1 (green) and AtMSH4 (magenta), to monitor the localization of DSBs on the axial elements. In both wild-type and *des10* early (RAD51 and DMC1) and intermediate (MSH4) recombination proteins load on the chromosome axis (ASY1) revealing that crossing over intermediates are formed in both wild-type and *des10*. Scale bars 5µm.